HHS Public Access

Author manuscript

Curr Biol. Author manuscript; available in PMC 2019 January 22.

Published in final edited form as:

Curr Biol. 2018 January 22; 28(2): 236–248.e5. doi:10.1016/j.cub.2017.12.007.

Opposing Kinesin and Myosin-I Motors Drive Membrane Deformation and Tubulation along Engineered Cytoskeletal Networks

Betsy B. McIntosh[1,2], **Serapion Pyrpassopoulos**[1,2], **Erika L.F. Holzbaur**[1,2,*], and **E. Michael Ostap**[1,2,3,*]

[1]The Pennsylvania Muscle Institute and Department of Physiology, Perelman School of Medicine, University of Pennsylvania, Philadelphia, PA 19104-6085, USA

[2]Center for Engineering MechanoBiology, University of Pennsylvania, Philadelphia, PA 19104-6085, USA

SUMMARY

Microtubule and actin filament molecular motors such as kinesin-1 and myosin-Ic (Myo1c) transport and remodel membrane-bound vesicles; however, it is unclear how they coordinate to accomplish these tasks. We introduced kinesin-1- and Myo1c-bound giant unilamellar vesicles (GUVs) into a micropatterned in vitro cytoskeletal matrix modeled after the subcellular architecture where vesicular sorting and membrane remodeling are observed. This array was composed of sparse microtubules intersecting regions dense with actin filaments, and revealed that Myo1c-dependent tethering of GUVs enabled kinesin-1-driven membrane deformation and tubulation. Membrane remodeling at actin/microtubule intersections was modulated by lipid composition and the addition of the Bin-Amphiphysin-Rvs-domain (BAR-domain) proteins endophilin or FCH-domain-only (FCHo). Myo1c not only tethered microtubule-transported cargo, but also transported, deformed, and tubulated GUVs along actin filaments in a lipid-composition- and BAR-protein-responsive manner. These results suggest a mechanism for actin-based involvement in vesicular transport and remodeling of intracellular membranes, and implicate lipid composition as a key factor in determining whether vesicles will undergo transport, deformation, or tubulation driven by opposing actin and microtubule motors and BAR-domain proteins.

In Brief

[*]Correspondence: holzbaur@pennmedicine.upenn.edu (E.L.F.H.), ostap@pennmedicine.upenn.edu (E.M.O.).
[3]Lead Contact

SUPPLEMENTAL INFORMATION

Supplemental Information includes two figures and nine movies and can be found with this article online at https://doi.org/10.1016/j.cub.2017.12.007.

DECLARATION OF INTERESTS

The authors declare no competing interests.

AUTHOR CONTRIBUTIONS

B.B.M., E.M.O., and E.L.F.H. designed experiments, wrote and edited the paper, and secured funding. B.B.M. performed and analyzed all experiments except those contributing to Figure S1B and Movie S2. S.P. edited the paper, provided technical expertise, performed foundational experiments for Myo1c-driven motility, and contributed Figure S1B and Movie S2.

McIntosh et al. engineer cytoskeletal arrays containing dense actin networks interconnected by sparse microtubules, and demonstrate that Myo1c and kinesin-1 transport, deform, and tubulate large unilamellar-membrane vesicles. Further, they find that BAR-domain proteins and lipid composition modulate motor-driven changes in vesicle morphology.

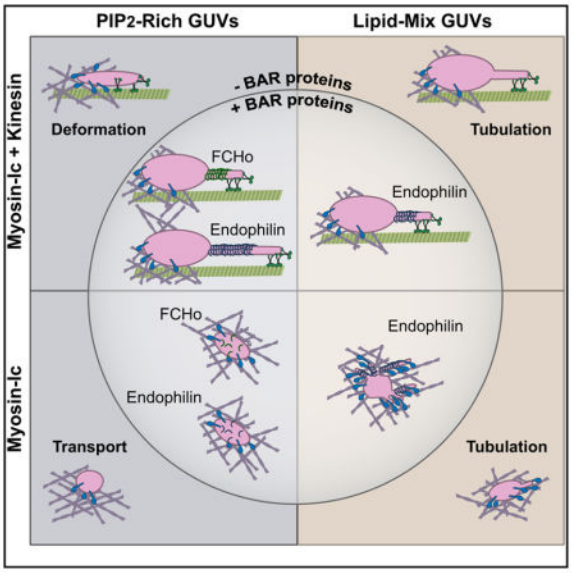

INTRODUCTION

Molecular motors transport and remodel vesicular cargos along microtubule (MT) and actin filament (AF) tracks. Long-distance transport from the cell center to the periphery occurs primarily along sparse, radially oriented MT tracks, but there is substantive overlap of MTs with AFs in regions of dynamic membrane remodeling [1–4]. This overlap is particularly important for organelle tubulation and cargo sorting during intracellular trafficking, for instance from recycling endosomes near the cortex and at the *trans*-Golgi. AFs are known to contribute to the structural integrity of sorting compartments, and may also facilitate membrane deformation and tubulation through myosin motor activity. Although both MT- and AF-based motors are implicated in dynamic membrane remodeling events, the interplay between these factors is not yet clear [5–10].

To better understand the roles of AF and MT motors in the transport and deformation of membrane-bound cargos, we used microfabrication laser-patterning techniques to engineer a cytoskeletal geometry *in vitro* that models the cytoskeletal overlap zones where membrane remodeling occurs within the cell: sparse MTs crossing dense AFs [2, 3]. We used this system to explore the interplay between the MT motor kinesin-1 and the membrane-associated AF motor myosin-Ic (Myo1c), as these motors have been implicated in cellular pathways resulting in membrane tubulation [6, 11–14]. By analyzing the shape and motility of deformable membrane-bound cargo in a physiologically relevant cytoskeletal array, we explored the dynamics of deformation and tubulation and asked how BAR-domain (Bin-Amphiphysin-Rvs-domain) membrane-curvature-stabilizing factors, such as endophilin and FCHo (FCH-domain-only), influence the interplay between deformation and tubulation of

MT- and AF-driven cargo. We also probed the role of lipid-membrane composition in the interplay between transport, deformation, and tubulation of MT- and AF-driven cargo and BAR-domain protein scaffolding.

We find that Myo1c and kinesin-1 work together to deform PI(4,5)P_2-rich giant unilamellar vesicles (PIP_2-GUVs) along MTs at AF intersections, and tubulate GUVs when endophilin or FCHo, membrane-curvature-stabilizing BAR proteins, are present. These two types of BAR proteins both enhance tubulation along MTs by kinesin-1 and induce deformation and tubulation along AFs by Myo1c. In contrast, we find that kinesin-1 and Myo1c alone are sufficient to readily tubulate GUVs that have a composition that more closely mimics the inner leaflet of the plasma membrane and recycling endosomal compartments. Moreover, this physiological lipid mixture (LM-GUVs) results in robust Myo1c-driven tubulation along AFs. These findings implicate myosin-I motors as an effector of AF-induced membrane remodeling and transport. Additionally, our results demonstrate that lipid composition substantially impacts the ability of AF and MT molecular motors to power membrane remodeling.

RESULTS

Kinesin-1 and Myo1c Transport PI(4,5)P_2-Rich GUVs (PIP_2-GUVs) along MTs and AFs

To investigate membrane deformation and tubulation *in vitro* in a physiologically relevant model of the cellular cytoskeleton, we used laser micropatterning to oxidize PEG-silane-coated coverslips in approximately 3-μm-wide stripes, separated by 20 μm, to which NeutrAvidin was tightly adsorbed (Figure 1A) [15]. The coverslip was assembled into a glass flow chamber, and a solution of biotinylated, Taxol-stabilized MTs was introduced by flowing perpendicular to the stripe pattern. After MTs bound to and spanned the stripes, a solution of biotinylated, phalloidin-stabilized AFs was subsequently introduced, resulting in a cytoskeletal array with MTs beneath AFs (see STAR Methods for details). Myo1c was attached to PIP_2-GUVs via its physiological binding interaction with PI(4,5)P_2, whereas His-tagged kinesin-1 bound to the NTA(Ni)-functionalized lipid (NTA, nitrilotriacetic acid; see Table 1; PIP_2-GUVs for lipid composition) [16–18]. Because kinesin-1 localizes to intracellular cargo in low motor numbers, we chose to use a dilute solution concentration (10 nM) [19]. At this concentration of kinesin-1, we observe prolific transportation of membrane-bound cargo but do not observe spontaneous tubulation along MTs. The GUVs, motor(s), and an ATP-containing activation buffer were then perfused into the flow cell for observation by total internal reflection fluorescence (TIRF) microscopy. Use of TIRF microscopy significantly improved the signal-to-noise ratio of membrane deformation and tubulation by illuminating only the ~200 nm of the GUV closest to the coverslip.

PIP_2-GUVs were actively transported along MTs by kinesin-1, and were observed to pause at AF/MT intersections in 30% of events in the absence of Myo1c. In contrast, kinesin-1-driven transport halted in 100% of events at AF/MT intersections in the presence of Myo1c (Figure 1B). These results are consistent with findings from previous experiments in which kinesin-1 and Myo1c motors were attached to non-deformable membrane-coated beads via a biotin-lipid-NeutrAvidin complex [20]. Also as found previously, there was an increase in

the percentage of kinesin-1-driven MT-based runs that initiated at AF intersections in the presence of Myo1c (Figure 1C).

Surprisingly, 24% of kinesin-1-driven runs in the presence of kinesin-1 and Myo1c initiate motility along AFs, then switch to motility along MTs (Figures 1C and S1A; Movie S1). Although Myo1c has been implicated as a slow-moving vesicular transporter within cells, this is the first *in vitro* reconstitution of Myo1c-driven vesicle motility. We hypothesize that the dynamic, physiological attachment of Myo1c to $PI(4,5)P_2$ is required for robust Myo1c-driven transport, because this motility was not observed when truncated Myo1c was attached to membrane-coated beads using a biotin-NeutrAvidin interaction [20]. In support of this hypothesis, we were able to reproduce full-length Myo1c-driven motility of membrane-coated beads in an ATP-dependent manner, even at $PI(4,5)P_2$ mole-percentages as low as 2% (Figure S1B; Movie S2). Distance versus time plots (Figure 1D) show that Myo1c-driven motility of GUVs is characterized by long periods of slow motility (<20 nm/s) and pauses, interspersed with short periods of faster motility (>50 nm/s). This motility is easily distinguishable from the approximately 100-fold faster kinesin-1-driven, MT-based transport. Figure 1D (orange line) shows an example event that switched from 13 nm/s Myo1c-driven AF-based transport to 410 nm/s kinesin-1-driven MT-based transport, where the dashed portion of the line demarcates the MT-driven motility. We find that Myo1c-driven cargos are transported along AFs at a median velocity of 6.0 nm/s (Figure 1E), and appear to continue motility to the end of AF tracks.

Myo1c and Kinesin-1 Deform PIP_2-GUVs along the MT at AF/MT Intersections

We hypothesized that Myo1c-driven tethering of kinesin-1-transported cargo at AF/MT intersections could provide the resistive force necessary for kinesin-1 to effectively deform or tubulate a GUV along the MT. Thus, we measured the deformation of GUVs along the MT as they encountered AF intersections during MT-based transport. PIP_2-GUV deformation was quantified by measuring, via a kymograph drawn along the MT, the length of the GUV as it changed shape over time. We expressed these measurements as a ratio of the longest over the shortest measurements, termed β. Kinesin-1-only PIP_2-GUVs were largely non-deformed at AF/MT intersections, with a mean β of 1.12 ± 0.120 (Figure 2A; Movie S3). We defined “deformation” as a β value greater than that observed in 95% of all events, or two SDs from the mean, for kinesin-1-only membrane shape changes ($\beta \geq 1.36$). In the presence of both kinesin-1 and Myo1c, there was a significant increase in the magnitude of deformation observed at AF/MT intersections, with a mean β of 1.68 ± 0.720. Here, 57% of all GUVs at AF/MT intersections deformed in the presence of both motor types (Figure 2B; Movie S3), in contrast to 5% of kinesin-1-only PIP_2-GUVs. Tubulation events along MTs, as defined by the elongation of membrane extensions of a diffraction-limited width, were rare (3% of events), although deformation and tubulation of the same GUV were occasionally observed (Figure 2C; Movie S4). In this example, the GUV translocated along an AF to an AF/MT intersection, deformed upon initiation of MT-based transport, and then dynamically tubulated along the MT at a second AF/MT intersection. The shape parameters of the GUVs shown in Figures 2A–2C are summarized in Figure 2D.

We hypothesized that the increase in membrane deformation along MTs observed when both motor types are present is facilitated by Myo1c-dependent tethering at AF intersections. To determine whether a static, non-motor anchor could similarly induce kinesin-1-driven membrane deformation, we replaced the Myo1c-AF interaction with a lipid-biotin-NeutrAvidin anchor. We added 10% biotinylated lipid to the PIP_2-GUV mixture (biotin-PIP_2-GUVs; Table 1), allowing direct tethering of GUVs to NeutrAvidin stripes along the coverslip (Figure S2A). We measured the pausing time for GUVs encountering these stripes, and found that biotin-PIP_2-GUVs pause for a median length of 13.8 s, which is shorter than the median pause length of 31.0 s induced by Myo1c but longer than the pauses observed for kinesin-1-only GUVs encountering AF intersections (8.00 s) (Figure S2B). Biotin-PIP_2-GUVs deform less frequently than kinesin-1+Myo1c-coated PIP_2-GUVs (19% versus 57%, respectively) but tubulate nearly four times more frequently than PIP_2-GUVs along MTs (11% versus 3%, respectively). Deformation and tubulation were not observed in kinesin-1-transported GUVs that failed to tether at NeutrAvidin stripes. These results indicate that the dynamic tethering of GUVs to AF intersections by Myo1c is required for robust membrane remodeling.

Myo1c and BAR Proteins Coordinate to Enhance Kinesin-1-Driven Tubulation of PIP_2-GUVs along MTs

BAR-domain proteins bind, stabilize, and tubulate membranes *in vivo* and *in vitro* [21–24]. Endophilin-A1 is an N-BAR-domain protein with an N-terminal helix that directly inserts into the lipid bilayer, enhancing electrostatic interactions between the protein and membrane [25]. Endophilin-A1 functions in endocytosis, exocytosis, and membrane trafficking of early, late, and recycling endosomes [21, 26–29]. *In vitro*, the N-terminal domain of endophilin-A1 (endophilin N-BAR) binds to and stabilizes highly curved membranes when present at concentrations in the nanomolar range; the same protein can generate membrane curvature, tubulate GUV membranes, and cause membrane scission at micromolar concentrations [24, 30–32]. Because cellular concentrations of endophilin are thought to be nanomolar [23, 33], we examined the effects of 8 and 80 nM endophilin N-BAR on membrane remodeling by kinesin-1 and/or Myo1c. When kinesin-1 but not Myo1c was attached to PIP_2-GUVs, vesicles did not deform along MTs even in the presence of endophilin. In contrast, when both kinesin-1 and Myo1c were present, endophilin caused a concentration-dependent increase in the frequency of GUV tubulation at AF/MT intersections (Figures 3A and S2C; Movie S5).

Next, we compared these observations to the effects of FCHo-2, an F-BAR protein thought to function upstream of endophilin in endocytic-signaling cascades, at or before the initiation of tubulation [34–36]. FCHo binds to $PI(4,5)P_2$ and other acidic phospholipids, and localizes to phosphoinositide-rich membranes and the inner leaflet of the plasma membrane [36, 37]. FCHo and endophilin induced similar levels of kinesin-1-driven tubulation, but the kinetics and morphology of the tubes differ (Figures 3B–3D; Movie S6). In the presence of Myo1c and 80 nM endophilin, kinesin-1 slowly (420 ± 250 nm/s) elongated long tubes (up to 46 μm) that persisted over ~33 s. In contrast, 80 nM FCHo facilitated more rapid kinesin-1-driven tubulation events (630 ± 250 nm/s), where tubes were shorter (up to 11 μm) and persisted for a shorter period of time (~17 s) (Figures 3D and 4).

Although both endophilin and FCHo significantly increased deformation (β) and tube elongation (Figures 4A and 4B), endophilin-facilitated tubes were significantly longer than FCHo tubes (Movie S5). Of note, in our assays, tubulation length was rarely limited by MT length, because the kinesin motors pulling the tube could switch between tracks (Movie S5).

Both endophilin and FCHo significantly increased the velocity of kinesin-1-driven tube elongation, although the effects of FCHo were more pronounced (Figure 4C). However, even at the highest concentration of FCHo examined, tube extension velocities were not as fast as those observed for a single kinesin-1 processing along an MT under similar assay conditions (Figure 4C). Although FCHo tubulation events elongated faster, they persisted for shorter times than those stimulated by endophilin (Figure 4D).

Myo1c-Driven Transport and Membrane Remodeling along AFs Are Modulated by Endophilin and FCHo

GUVs are not deformed along AFs during Myo1c-driven transport in the absence of BAR-domain proteins (Figure 5A). On each GUV, an ensemble of Myo1c motors navigates the dense, non-polarized and non-crosslinked, AF network. This motility typically continues to the end of AFs, or until encountering and switching to MT-based transport (Figures 1C and S1A). Endophilin and FCHo increased Myo1c-driven deformation along AFs from 12% to 34% (Figure 5B). We also observed Myo1c-driven tubulation in the presence of either BAR protein (Figures 5C–5E).

We found that FCHo induces morphologically dynamic changes in PIP_2-GUVs, independent of their interaction with the cytoskeleton. Morphologically dynamic GUVs strikingly tubulated along AFs, often into multiple tubular extensions (Figures 5C and 5E). These morphologically dynamic GUVs were not observed in the presence of 80 nM endophilin on PIP_2-GUVs, suggesting that FCHo, but not endophilin, may alter the baseline morphology of GUVs prior to force generation by cytoskeletal motors. When examining only the spherical PIP_2-GUVs, we found that addition of either 80 nM endophilin or 80 nM FCHo significantly increased the deformation of Myo1c-driven GUVs along AFs (Figure 5F).

GUVs Composed of a Physiological Lipid Mixture (LM-GUVs) Promote Tubulation along Both MTs and AFs by Kinesin-1 and Myo1c

The composition of a lipid-membrane-bound compartment has been proposed to alter motility driven by AF and MT motors. *In vitro*, lipid fluidity has been shown to decrease MyoV-driven liposome velocities [38] and enhance dynein motor cooperativity for longer runs and higher force-generation properties [39]. Yet, it is still unknown how lipid composition affects the interplay between AF- and MT-based motors, as well as BAR-protein scaffolding, in transport and tubulation. The experiments detailed above used mole fractions of $PI(4,5)P_2$ to mimic phosphoinositide-rich lipid microdomains [40, 41], in keeping with previous work [42]. To extend our studies, we investigated the deformation of GUVs composed of a lipid mixture (LM-GUVs) that better mimics the inner leaflet of the plasma membrane and recycling endosomes (LM-GUVs; Table 1) [43–49].

Changing the lipid composition from PIP_2-GUVs to LM-GUVs drastically increased the frequency of kinesin-1-driven tubulation at Myo1c-tethered AF intersections. In the absence

of endophilin, PIP_2-GUVs tubulated along MTs at 3% of all AF/MT intersections, whereas LM-GUVs tubulated along MTs at 52% of intersections (Figure 6A compared to Figure 3C). Addition of endophilin to LM-GUVs did not induce a significant increase in deformation or tubulation frequencies (Figure 6A). These kinesin-1-driven tubulation events show strikingly different dynamics compared to PIP_2-GUVs in the presence or absence of BAR proteins (Figure 4). Of note, LM-GUV tubulation events elongate at a significantly faster velocity than PIP_2-GUVs, even when endophilin or FCHo is present (Figure 4C). These LM-GUV tube-elongation velocities are comparable to single-molecule kinesin-1 velocities under the same buffer and imaging conditions (Figure 4C). Additionally, faster tube-elongation velocities inversely correlate with tube lengths (Figure 4B) and tube persistence time (Figure 4D), similar to PIP_2-GUV-based FCHo tubulation.

In addition to deformation and tubulation along MTs, we observed substantial membrane remodeling of LM-GUVs along AFs. In one striking example, an LM-GUV first tubulated along AFs by Myo1c, and then switched to kinesin-1-driven MT-based tubulation (Figure 6B; Movie S7). Notably, a large proportion of LM-GUVs were irregularly shaped and morphologically dynamic as they encountered the cytoskeleton (Figures 6C–6E). Unlike PIP_2-GUVs, most LM-GUVs deformed or tubulated during AF-based transport (compare Figure 6C to Figure 5E). Along AFs, addition of endophilin to LM-GUVs significantly increased tubulation of morphologically dynamic and spherical vesicles (Figure 6C). In contrast, PIP_2-GUVs were spherical and predominantly non-deformed (Figure 5E). Overall, we observed a significant increase in the deformation (β) of spherical LM-GUVs compared to PIP_2-GUVs along AF tracks (Figure 5F).

We also examined the dynamics of LM-GUVs with 25% cholesterol added to the lipid mixture (CH-LM-GUVs; see Table 1 for lipid composition) [43–48]. Addition of cholesterol destabilized the GUVs, resulting in less than half as many MT-based transport events over roughly equal numbers of GUV preparations and fields of view observed (18 events for the 0 nM endophilin condition; 8 events for the 80 nM endophilin condition). Based on limited observations, we noted that similar to LM-GUVs, approximately 50% of CH-LM-GUVs tubulated along MTs at AF intersections (compare to Figure 6A). Tube lengths were equivalent for CH-LM-GUVs and LM-GUVs, but tubulation velocities were slower (CH-LM-GUVs: 770 ± 250 nm/s versus LM-GUVs: 910 ± 260 nm/s).

Cholesterol-induced GUV destabilization was also observed as a significant decrease in Myo1c-driven transport along AFs (48 events for the 0 nM endophilin condition; 90 events for the 80 nM endophilin condition). We observed less frequent Myo1c-driven tubulation than LM-GUVs (13% versus 26%, respectively). Interestingly, tubulation frequency was not increased by addition of endophilin (14%), which was observed with LM-GUVs (50% tubulated) (Figure 6C). Although cholesterol decreases the frequency of tubulation, when comparing only spherical GUVs, CH-LM-GUVs deform with a similar magnitude (β) to LM-GUVs. Thus, cholesterol doesn't significantly alter MT-based or AF-based deformation and tubulation of LM-GUVs.

DISCUSSION

MT-Based Tubulation

In many cell types, the cytoskeleton is organized with MTs radiating outward from the centrosome toward the cell periphery, where endosomal recycling occurs [1–4]. AFs are concentrated at endoplasmic reticulum (ER)- and *trans*-Golgi-exit sites [7–9], and beneath the plasma membrane at sites of endocytosis and endosomal recycling [3, 6, 10]. Thus, there is substantial overlap of MTs and AFs in regions of active intracellular sorting and membrane remodeling. This geometry suggests a role for both MT- and AF-based motors in membrane remodeling. Here, we used micropatterning to engineer intersecting cytoskeletal arrays to model the cellular architecture and test how motors cooperate to power changes in membrane morphology (Figure 1A).

We found that Myo1c effectively anchors kinesin-1-driven cargo at AF/MT intersections, resulting in membrane deformation and tubulation along MTs (Figures 1B, 2, and 3C). Tubulation along MTs is rare in the absence, and enhanced in the presence, of the BAR-domain proteins endophilin or FCHo (Figure 3C). Although a static, non-motor anchor can increase the frequency of kinesin-1-driven tubulation, significantly less membrane deformation occurred under these conditions (Figures S2B and S2C). These findings suggest that tethering of kinesin-1-driven cargo by Myo1c favors membrane deformation, and that active tethering modulates the level of membrane remodeling.

Kinesin-1-driven tubulation of Myo1c-tethered GUVs is differentially stimulated by endophilin based on lipid composition (summarized in Figure 6F). Addition of endophilin induced a significant increase in the frequency of tubulation of PIP_2-GUVs, but not LM-GUVs, along MTs (Figures 3C and 6A). We hypothesize that endophilin enhances tubulation by stabilizing transient membrane curvature generated by motors, effectively lowering the resisting load experienced by kinesin-1. This is supported by the observed increase in tubulation velocities when endophilin is present (Figure 4C). In contrast, the irregular and dynamic shapes of LM-GUVs suggest a higher inherent deformability of these vesicles, which may explain the lack of additional tubulation induced by endophilin (Figure 6A). No additional membrane-deformation factors appear to be necessary for kinesin-1 to induce robust membrane tubulation of LM-GUVs. We also note that nanomolar endophilin concentrations induced little to no tube scission in our assays, similar to previous observations [32].

The ability of a highly processive motor like kinesin-1 to tubulate reconstituted and purified membranes has been well characterized (for example, [50–52]). It is estimated to take 20–30 pN of force to pull a tube out of a lipid membrane, and thus it is expected to take four to six kinesin-1 motors to initiate and elongate a tubulation event [53–56]. Because kinesin-1 motors typically pull a tube from its tip [54, 57], motor detachment due to mechanical or kinetic limitations will result in the retraction of a tube. Here we show that Myo1c can stabilize elongated tubes at AF intersections, preventing tubulation events from retracting back to the GUV body. Kinesin-1-driven tube-elongation velocities suggest that LM-GUVs offer an extremely low resistance to tubulation, and thus individual kinesin-1 motors are most likely pulling tubes along MTs very near their unloaded velocities. This may explain

the shorter run lengths and higher frequencies of tubulation of these GUV populations (Figure 4). Similarly, the BAR-domain proteins endophilin and FCHo are able to lower the effective force barrier of kinesin-1-driven tubulation of PIP_2-GUVs to increase both the frequency of tubulation and the tube-elongation velocities [23, 24, 35].

AF-Based Tubulation

Myo1c robustly transports PIP_2-, LM-, and CH-LM-GUVs along individual and densely patterned AFs (Figures 1, 5, and 6). Addition of endophilin or FCHo increases the fraction of deformed and tubulated GUVs along AFs (Figure 5E). This deformation and tubulation was unexpected, because we predicted that GUVs navigating a dense, non-polarized AF network would stall at AF/MT intersections. These results also demonstrate that Myo1c can tubulate along single AFs, without the need for bundles, as proposed for Myo1b [42].

Although endophilin and FCHo differentially enhance kinesin-driven PIP_2-GUV tubulation, we observed that these two BAR proteins similarly affect Myo1c-driven membrane remodeling (Figures 5E and 5F). By varying the lipid composition to a more physiological mixture (LM-GUVs), we stimulated increased tubulation along AFs, but this increase in tubulation was attenuated in CH-LM-GUVs (Figure 5F). LM-GUVs show robust tubulation of morphologically dynamic GUVs by Myo1c, even without endophilin present.

Unlike in the case of kinesin-1-driven membrane remodeling, spherical and morphologically dynamic LM-GUV tubulation was further increased by addition of endophilin (Figure 6C). This increase in AF-based, but not MT-based, tubulation suggests that the processive kinesin-1 and non-processive Myo1c are differentially affected by membrane deformability. The varied morphology of LM-GUVs suggests increased deformability of the membrane, which may promote tubulation along AFs. Because we observed a significant increase in tubulation along AFs in the presence of endophilin, we suggest that endophilin stabilizes already-curved membranes, promoting further Myo1c-driven membrane remodeling.

Myo1c is an active effector of AF-based deformation and tubulation (Figures 5 and 6); a passive tether does not result in these membrane remodeling events. Unlike Myo1b, which becomes tightly bound to AFs as a force-responsive catch bond, the ATPase kinetics of Myo1c are less sensitive to mechanical load [58, 59]. Thus, despite having 100-fold slower ATPase activity than kinesin-1 [55], Myo1c is not acting as a rigor-bound tether to kinesin-1-driven cargo but rather is acting as a dynamic AF docking team [20, 60].

Lipid Composition Affects Transport, Deformation, and Tubulation of AF- and MT-Based Cargo

Varying lipid composition by using cholesterol or acyl-chain variability can affect vesicular cargo transport by molecular motors [38, 39, 61]. Here we show that varying lipid head-group composition can alter the ability of both kinesin-1 and Myo1c to deform and tubulate membranes along their respective tracks. BAR-domain proteins also enhance the deformability of GUVs. Data of GUV remodeling along AFs suggest that lipid composition may impact baseline GUV deformability more than the particular BAR protein present.

FCHo enhanced kinesin-1-driven tubulation at faster velocities but with shorter persistence times compared to endophilin. This suggests that FCHo binds to and detaches from membranes faster than endophilin. These properties parallel the roles of FCHo and endophilin in endocytic-signaling and membrane-deformation cascades, where FCHo binds to relatively non-curved surfaces to initiate membrane deformation and endophilin binds later to highly curved membranes to stabilize and facilitate membrane scission [28].

The ability of endophilin to tubulate GUVs *in vitro* when in the micromolar protein range has been difficult to connect to cellular observations, where protein concentrations are ~0.1 μM [23]. Here we show that low-nanomolar concentrations of endophilin N-BAR enhance kinesin-1-driven tubulation in PIP_2-GUVs, and Myo1c-driven tubulation in LM-GUVs (Figure 3C). Additionally, these results comparing FCHo- and endophilin-facilitated tubulation indicate that BAR proteins may be generally available to pair with molecular motors to facilitate membrane remodeling, with each BAR protein differentially altering the dynamicity of remodeling membranes (Figure 6F, summary). Our results suggest that the membrane dynamics of BAR proteins influence properties of tubulation events, and indicate that different BAR proteins, or combinations of BAR proteins, may be used to modulate tubulation events in space and time.

Conclusions

We show that both Myo1c and kinesin-1 are capable of transporting, deforming, and tubulating GUV membranes along their respective cytoskeletal tracks. Kinesin-1-driven deformation and tubulation are enabled by Myo1c tethering to AF/MT intersections, connecting the AF and MT cytoskeletal regimes to membrane remodeling. This supports the hypothesis that the AF cytoskeleton is affecting vesicular transport and remodeling through myosin motor intermediates. We also provide evidence that Myo1c, a non-processive single-headed motor, can remodel vesicular cargo membranes, both alone and in conjunction with powerful and processive MT-based transporters like kinesin-1. This deformation of AF-transported cargo by Myo1c is highly dependent upon the presence of BAR-domain stabilization of curved membranes and/or the lipid composition of these transported membranes. On the other hand, kinesin-1-driven tubulation is differentially enhanced by BAR-protein scaffolding depending on the lipid composition of the cargo. Crucially, our results show that it is essential to consider the interplay between opposing MT- and AF-based molecular motors and the influence of lipid-composition and BAR-protein scaffolding in cargo transport and membrane remodeling.

STAR★METHODS

Detailed methods are provided in the online version of this paper and include the following:

KEY RESOURCES TABLE

REAGENT or RESOURCE	SOURCE	IDENTIFIER
Bacterial and Virus Strains		
Myo1c motor C baculovirus (pLT16)	Ostap Laboratory	N/A

REAGENT or RESOURCE	SOURCE	IDENTIFIER
Biological Samples		
Microtubules purified from bovine brain	Bovine brain [62]	N/A
Chemicals, Peptides, and Recombinant Proteins		
Human kinesin-1 (KIF5B) from E.coli amino acids 1-506	Ron Vale [63]	N/A
Mouse full-length Myo1c (Myo1c-FLAG)	Mouse cDNA [64]	N/A
Rat endophilin-A1 N-BAR, amino acids 1-247; E241C for fluorescent labeling	Gift from Tobias Baumgart [65, 66]	N/A
Human FCHo2, amino acids 3-265, C86S, C147S, N240C for single-cysteine mutant fluorescent labeling	Gift from Harvey McMahon [35] via Tobias Baumgart	N/A
Chicken calmodulin	Chicken [67]	N/A
Human platelet G-actin (> 99% pure)	Cytoskeleton, Inc.	Cat#APHL99-A
Alexa Fluor 488	Life Technologies	Cat#A12379
Biotin-xx phalloidin	Life Technologies	Cat#B7474
HiLyte 647 porcine brain tubulin	Cytoskeleton, Inc.	Cat#TL2670M
Biotin-labeled porcine brain tubulin	Cytoskeleton, Inc.	Cat#T333P
Paclitaxel	Cytoskeleton, Inc.	Cat#TXD01
porcine brain L-α-phosphatidylinositol-4,5-bisphosphate	Avanti Polar Lipids	Cat#840046X
18:1 1,2-dioleoyl-*sn*-glycero-3-[(N-(5-amino-1-carboxypentyl)iminodiacetic acid)succinyl] (nickel salt)	Avanti Polar Lipids	Cat#790404C
18:1 1,2-dioleoyl-*sn*-glycero-3-phosphoethanolamine-N-(lissamine rhodamine B sulfonyl) (ammonium salt)	Avanti Polar Lipids	Cat#810150C
18:1 (Δ9-Cis) 1,2-dioleoyl-*sn*-glycero-3-phosphocholine	Avanti Polar Lipids	Cat#851375C
1,2-dioleoyl-*sn*-glycero-3-phosphoethanolamine-N-(cap biotinyl)	Avanti Polar Lipids	Cat#870273C
18:1 (Δ9-Cis) 1,2-dioleoyl-*sn*-glycero-3-phosphoethanolamine	Avanti Polar Lipids	Cat#850725C
18:1 1,2-dioleoyl-*sn*-glycero-3-phospho-L-serine	Avanti Polar Lipids	Cat#840035C
1,2-dioleoyl-*sn*-glycero-3-phospho-(1′-myo-inositol) (ammonium salt)	Avanti Polar Lipids	Cat#850149P
Porcine brain sphingomyelin	Avanti Polar Lipids	Cat#860062C
Cholesterol (ovine wool)	Avanti Polar Lipids	Cat#110796
mPEG-silane, 30 k	Creative PEGWorks	Cat#PSB-2014
NeutrAvidin	Fisher Scientific	Cat#PI-31000
Poly(L-lysine)-graft-poly(ethylene glycol) co-polymer	SuSos	Cat#PLL(20)_-g[3.5]-PEG(2)
Phosphocreatine, disodium salt hydrate	Sigma-Aldrich	Cat#P7936
Creatine phosphokinase, Rabbit muscle	Sigma-Aldrich	Cat#C3755
Experimental Models: Cell Lines		
Sf9	Thermo Fisher	Cat#B82501
Software and Algorithms		
Volocity image acquisition software	PerkinElmer	SCR_002668
ImageJ	NIH	RRID:SCR_003070
Prism	GraphPad	SCR_002798
Other		
4–8 ohms resistance, 25×75×1, 1 mm ITO-coated glass slides	Delta Technologies	Cat#CG-401N-S115

CONTACT FOR REAGENT AND RESOURCE SHARING

Further information and requests for resources and reagents should be directed to and will be fulfilled by the Lead Contact, Michael Ostap (ostap@pennmedicine.upenn.edu).

EXPERIMENTAL MODEL AND SUBJECT DETAILS

Sf9 cells were obtained from a commercial distributor and grown following their instructions (Thermo Fisher; see Key Resources Table for details).

METHOD DETAILS

Reagents

Expressed and Purified Motor Proteins

Kinesin-1: We expressed and purified a human kinesin-1 (KIF5B) construct from *E. coli* [20], which contains the first 560 amino acids of the heavy chain sequence with a 6x-His tag and GFP added to the C terminus [63]. The DNA was transformed into Rosetta2 PlysS bacteria, and grown overnight at 37°C. Rosetta2 PlysS bacteria, and grown overnight at 37°C. Cultures were cooled down to 23°C for 0.15 mM IPTG-induced protein expression for 6–18 hr. Cells were flash frozen in liquid nitrogen and stored at −80°C. The day of purification, cells were lysed by French Press after resuspension in a lysis buffer, with 5 μg/mL DNase1 present. Lysate was pelleted, diluted in wash butter, and run over a Co^{2+} resin (Clontech) column at 1 mL/min. After washing and elution of the protein, the best fractions were determined by Coomassie gel, pooled, and concentrated. Buffer was exchanged to PEM (100 mM NaPIPES, 1 mM $MgSO_4$, 1 mM EGTA) by running sequentially over a Nap10 and PD10 exchange column. MT affinity/dead-head spin was performed by binding K560 to newly polymerized (taxol-stabilized, unlabeled microtubules) with AMPPNP, rinsing to remove un-bound motors, and then releasing from microtubules in the presence of 5 mM MgATP. In this work, the concentration of kinesin-1 refers to the amount of heavy chain dimer in solution. This construct was attached to lipid membranes through its His-tag to a NTA(Ni)-functionalized lipid (see below for more information).

Myosin-Ic: A full length mouse Myo1c isoform C (construct pLT16) was baculovirus expressed and purified from Sf9 cells as described in [64]. Sf9 cells were grown per instructions provided by the commercial distributor (Thermo Fisher). Briefly, Myo1c (pLT16) was cloned into baculovirus transfer vector pBlueBac4.5 (Invitrogen) and the recombinant baculovirus was generated using standard procedures (including plaque assay for selection).

Myo1c was co-expressed with calmodulin in Sf9 cells, which were harvested by centrifugation, flash-frozen in liquid nitrogen, and stored at −80°C until purification. Cells were resuspended in a lysis buffer and lysed with five strokes in a Dounce homogenizer, and centrifuged at 100,000 × g for 1 hr, and then sonicated with six 15 s pulses in the presence of 10 μg/mL RNase A (Roche) and 5 μg/mL DNase I (Roche). Myo1c was purified by running lysate over an Anti-FLAG M2 affinity resin (Sigma), washing, and eluting with 3x-FLAG peptide (Sigma) in the presence of calmodulin. Vertebrate calmodulin (CaM) was expressed and purified as described [67]. Eluent was dialyzed into HnA100 buffer (10 mM HEPES, pH

7.0, 100 mM NaCl, 1 mM DTT, and 1 mM EGTA) and aliquots were flash-frozen and stored in liquid nitrogen.

Expressed and Purified Endophilin and FCHo

Endophilin and FCHo: Rat endophilin A1 N-BAR was kindly cloned and purified by the laboratory of Tobias Baumgart at the University of Pennsylvania with residues 1-247 and an E241C substitution for fluorescent labeling, and purified as described [65, 66]. Note, all endophilin concentrations reported are the monomer concentration, yet, endophilin N-BAR exists as a dimer in solution [66]. Human FCHo2 was also kindly cloned and purified by the laboratory of Tobias Baumgart at the University of Pennsylvania, originally gifted by Harvey McMahon from MRC Laboratory of Molecular Biology in Cambridge, United Kingdom. This FCHo construct contains residues 3-265, with residues C86S, C147S, and N240C changed to create a single-cysteine mutant for fluorescent labeling and ease of purification. Both endophilin and FCHo were grown in BL21(DE3) RIL CodonPlus bacteria (Stratagene) overnight at at 37 °C, shaken at 225 rpm.

The purification protocol was as described [35]. Briefly, BL21DE3 codon plus cells (Strategene) were grown in an overnight starter culture at 37 °C, shaker set to 225 rpm. Protein expression was induced at O.D. ~0.5 with 1 mM IPTG and grown at 18°C for 16 hr while continuing to shake at 225 rpm. Lysate was clarified, and BAR proteins were purified using glutathione affinity, and run over a cation exchange column to purify FCHo, or an anion exchange column to purify endophilin. PreScission protease was used to cleave the GST-tag, and BAR proteins were purified further with a linear NaCl gradient and size exclusion chromatography (Superdex200, GE Healthcare).

Cytoskeleton Purification and Polymerization: Human platelet G-actin (> 99% pure) was purchased from Cytoskeleton, Inc. (Cat # APHL99-A), polymerized at a concentration of 2 μM and stabilized with either 1.33 μM Alexa Fluor 488 phalloidin (Life Technologies, Cat # A12379) and 0.57 μM biotin-xx phalloidin (Life Technologies, Cat # B7474) or 0.57 μM Alexa Fluor 488 phalloidin, 0.57 μM biotin-xx phalloidin, and 0.76 μM unlabeled phalloidin (Thermo Fisher Scientific, Cat # P3457) in MB (50 mM MOPS pH 7.0, 125 mM KCl, 5 mM EGTA, 5 mM $MgCl_2$, and 1 mM DTT). Microtubules were assembled from 92% bovine brain tubulin [62], 5% HiLyte 647 porcine brain tubulin (Cytoskeleton Inc., Cat # TL2670M), and 3% biotin-labeled porcine brain tubulin (Cytoskeleton Inc., Cat # T333P) at 50 μM tubulin dimer, and stabilized with 40 μM paclitaxel (Cytoskeleton Inc., Cat # TXD01) in BRB80 (80 mM K-PIPES, 1 mM $MgCl_2$, 1mM EGTA, at pH 6.8).

Lipids Utilized in Reconstituted Membranes

PIP_2-GUVs: PIP_2-GUVs were formed as described below (Table 1) following previous work by [42], and composed of 20.5% porcine brain L-α-phosphatidylinositol-4,5-bisphosphate (referred to as $PI(4,5)P_2$) (Avanti Polar Lipids, Cat # 840046X), 2.5% 18:1 1,2-dioleoyl-*sn*-glycero-3-[(N-(5-amino-1-carboxypentyl)iminodiacetic acid)succinyl] (nickel salt) (referred to as DGS-NTA(Ni)) (Avanti Polar Lipids, Cat # 790404C), 0.5% 18:1 1,2-dioleoyl-*sn*-glycero-3-phosphoethanolamine-N-(lissamine rhodamine B sulfonyl) (ammonium salt) (referred to as Rho-PE) (Avanti Polar Lipids, Cat # 810150C), and 76.5%

18:1 (Δ9-*Cis*) 1,2-dioleoyl-*sn*-glycero-3-phosphocholine (Referred to as PC) (Avanti Polar Lipids, Cat # 851375C).

Biotin-PIP$_2$-GUVs: Biotin-PIP$_2$-GUVs were composed of 10% 1,2-dioleoyl-*sn*-glycero-3-phosphoethanolamine-N-(cap biotinyl) (sodium salt) (referred to as biotin-PE) (Avanti Polar Lipids, Cat # 870273C), 66.5% PC, 20.5% PI(4,5)P$_2$, 2.5% DGS-NTA(Ni), and 0.5% Rho-PE.

Lipid Mix GUVs: Lipid Mix GUVs (LM-GUVs) were composed of 43.3% 18:1 (Δ9-*Cis*) 1,2-dioleoyl-*sn*-glycero-3-phosphoethanolamine (referred to as PE) (Avanti Polar Lipids, Cat # 850725C), 18.4% PC, 18.4% 18:1 1,2-dioleoyl-*sn*-glycero-3-phospho-L-serine (referred to as PS) (Avanti Polar Lipids, Cat # 840035C), 9.2% 18:1 1,2-dioleoyl-*sn*-glycero-3-phospho-(1′-myo-inositol) (ammonium salt) (referred to as PI) (Avanti Polar Lipids, Cat # 850149P), 4% porcine brain sphingomyelin (Avanti Polar Lipids, Cat # 860062C), 3.0% PI(4,5)P$_2$, 2.5% DGS-NTA(Ni), and 0.5% Rho-PE. CH-LM-GUVs were composed of 25% Cholesterol (ovine wool) (Avanti Polar Lipids, Cat #110796), 10.5% PC, 29.5% PE, 21% PS, 4.5% sphingomyelin, 4.5% PI, 2.0% PI(4,5)P$_2$, 2.5% DGS-NTA(Ni), 0.5% Rho-PE.

Preparation for in vitro Experiments

Preparation of Giant Unilamellar Vesicles (GUVs): GUVs were prepared by mixing the lipids (described above) to 0.973 mM in chloroform, warming to 37°C, thinly spreading on 37°C-warmed Indium-Tin-Oxide (ITO) slides (4–8 ohms resistance, 25×75×1, 1 mm ITO-coated glass slides, Delta-technologies #CG-401N-S115), and then drying in a vacuum desiccator for 2 hr or overnight. Next, lipid-coated slides were sandwiched with 300 mM sucrose in diH$_2$O and electroformed for 2.5 hr at 4 V peak-to-peak and 5 Hz at 60°C [65, 68]. GUV preparations were examined before use by applying 5 μL undiluted GUVs on to a glass coverslip and viewing via epifluorescence. Only GUV preps with large amounts of giant vesicles and few lipid aggregates (small or large) were used for experimentation. GUVs were used within 48 hr of formation and stored at room temperature.

Preparation of membrane-coated beads: Silica beads 0.54 μm in diameter (Bangs Laboratories, Inc) were coated with membranes containing 2% PI(4,5)P$_2$ and 98% PC. PC was mixed with 2 mol % of PI(4,5)P$_2$ in a 50-mL round-bottom flask. The solution was thermally equilibrated in a water bath at 35°C for 5 min and dried rapidly (~1 min) in a rotary evaporator. The lipid film was kept under hard vacuum for at least another 30 min. The lipid film was dissolved in 2 mL of HNa100 (2.5 mM total lipid concentration) and multilamellar vesicles were formed by vortexing the flask for 2 min. Lipid solution was subjected to 4 freeze-thaw cycles using dry ice and isopropanol (Fischer) mix for freezing and water bath at 37°C for thawing. Using a mini lipid extruder (Avanti Polar Lipids, Inc.) lipid solution was extruded at room temperature (RT) 11 times through 30 nm pores (polycarbonate membranes, Whatman) to form small unilamellar vesicles (SUVs). 40 μL of silica beads solution 9.83% solid (Bangs Laboratories, Inc) were washed as follows: (1) 1 mL methanol (Fisher), (2) 1 mL 1N KOH water bath sonication for 15 min, (3) 7 times with 1 mL of distilled H$_2$O. All washings were done on a benchtop centrifuge for 2 min, 735 g, at

RT (Centrifuge 5415C, Eppendorf). After the final washing beads were brought to their initial volume (~40 μL) and were mixed with 500 – 600 μL of SUVs. The mix of beads and SUVs was vortexed briefly at max speed and was let overnight at RT. The next day, beads were washed 3 times with 1 mL HNa100 (2 min, 735 xg, at RT) to a final volume of ~500 μL. Immediately before bead motility assays, 100 μL of lipid coated beads were transferred to motility buffer (60 mM MOPS, pH 7.0, 25 mM KCl, 1 mM EGTA, 1mM $MgCl_2$).

Preparation of patterned coverslips: Coverslip washing, coating, and patterning was adapted from [15, 69–71]. 24 × 40 mm #1.5 coverslips were rinsed with 100% ethanol, wiped with a Kimwipe, rinsed with running milliQ water for 15 min, and then dried in a filtered-air cell culture hood. Next, coverslips were bath-sonicated for 30 min at room temperature in acetone, rinsed with ethanol, and then incubated in 100% ethanol at room temperature for 10 min. Coverslips were then rinsed under running milliQ water for 10 min, and incubated in 2% Hellmanex III detergent for 2 hr or overnight. Finally, coverslips were vigorously rinsed with running milliQ water for 30 min and then dried in the filtered-air hood. For best results, coverslips were coated in PEG-silane (Creative PEGWorks, Cat # PSB-2014) and patterned within 48 hr. To coat with PEG-silane, coverslips were first plasma cleaned for 2 min, and then incubated in 1 mg/mL PEG-silane resuspended in 55% ethanol and 10 μL concentrated hydrochloric acid, diluted in diH_2O. Coverslips were incubated at room temperature on a gentle shaker, covered from light, overnight. The next morning, coverslips were rinsed 3 times in 100% ethanol, and then bath sonicated 3 × 5 min in 100% ethanol at room temperature, before being rinsed twice with diH_2O, and dried in filtered air hood.

Coverslips were patterned by using an IX-255 MicroX Excimer Laser at 193 nm in low fluence, RVA mode. A 7 mJ fiducial line was drawn perpendicular to the parallel pattern used in the cytoskeletal assay. Parallel lines were made with a 5 mJ laser intensity at highest attenuation (45°), an approximately 3.2 μm diameter, 1 burst-per-spot, 100 Hz laser rep-rate, with approximately 20 μm spacing between lines, and 20 lines per pattern (two patterns per coverslip). Coverslips were stored at room temperature in an amber-colored jar with desiccant and used for up to two weeks or until non-specific sticking on surface caused ablation of cytoskeletal patterning.

Experimental Procedures

In vitro reconstitution assay: Flow cells were assembled from patterned coverslips and cleaned glass slides formed into a chamber with double-stick tape to form 3 flow cells per coverslip with the pattern running perpendicular to flow cells. Each flow cell was treated as follows: (1) 25 μL of 0.25 mg/mL NeutrAvidin (Fisher Scientific, Cat # PI-31000) was incubated for 5 min; (2) 40 μL of casein wash buffer (30 mM DTT, 20 μM taxol, 15 μM CaM, and 1 mg/mL filtered casein diluted in pH 7.5 BRB80); (3) Poly(L-lysine)-graft-poly(ethylene glycol) co-polymer (referred to as PLL-PEG) (SuSos, Cat # PLL(20)_-g[3.5]-PEG(2)) was hydrated to 1 mg/mL in 10 mM HEPES (pH 7.4) and stored at 4°C for up to 1 week. 20 μL of 0.1 mg/mL PLL-PEG block was diluted in 10 mM HEPES pH 7.4 and flowed into chamber for 1 min incubation; (4) 40 μL casein block (30 mM DTT, 20 μM taxol in 5 mg/mL filtered casein diluted in pH 7.5 BRB80) for 5 min; (5) 20 μL 1:100 taxol-

stabilized microtubules with 3 × 30 s flows rapidly flowed into chamber (or to desired density on surface); (6) 3 × 20 μL washes with casein wash; (7) 20 μL of 1:10 phalloidin-stabilized F-actin incubated for 1 min (or to desired density on surface); (8) 3 × 20 μL flows of casein wash buffer; (9) 10 or 20 μL of GUV flow mixture, depending on desired vesicle density in chamber. GUV flow: 10 nM kinesin-1 (dimer concentration) +/− 200 nM Myo1c ± 8 or 80 nM endophilin/FCHo (monomer concentration), 3.7 μL diH_2O (to bring solution osmolarity to approximately 450 mOsm, which is slightly hypertonic to ~400mOsm electroformed GUV solution), 10 μL GUVs, and raised to 50 μL in Assay Buffer mixed (2.15 mM MgATP, 10 mM phosphocreatine (Sigma-Aldrich, disodium salt hydrate—P7936), 0.45 mg/mL creatine phosphokinase (Sigma-Aldrich, Rabbit muscle—C3755), 1.1 mg/mL glucose, 2.37 mM DTT, 15 μM CaM, 1 mg/mL filtered casein, diluted in BRB80 pH 7.5, and mixed with glucose-oxidase-catalase (Sigma-Aldrich, glucose oxidase from *Aspergillus niger* type VII—G2133, and catalase from bovine liver—C100) before being mixed with motors and GUVs and flowed into the chamber). Since MTs and AFs are only attached to the surface at the NeutrAvidin stripes, AFs are typically tacked down along their length within the NeutrAvidin stripe, while MTs are often only attached to the surface at their ends (or where they cross the patterned stripe). This occasionally resulted in MTs fluctuating in/out of the TIRF field, but generally did not influence analysis of GUV shape and behavior at AF/MT intersections.

In vitro assay for lipid membrane-coated bead motility by full length Myo1c along actin filaments: Glass coverslips 22 × 40-1.5 mm (12–544.B, Fisher Scientific) were coated with 4 μL of 0.1% solution of Nitrocellulose in Amyl Acetate (Electron Microscopy Sciences) and dried under a fume hood (~15 min). The Nitrocellulose coated coverslips were used to construct standard motility chambers [72] using double-sided tape and vacuum grease. Solutions were added to the chamber in the following sequence: (1) 20 μM actin-binding domain of α-actinin for 10 min, (2) 1 mg/mL casein for 3 min (3), 50 nM filamentous actin stabilized with Rhodamine Phalloidin in 1 mg/mL casein for 5 min, (4) washed with 1 mg/mL Casein, (5) mix of lipid-coated beads with 200 nM full length Myo1c, 10 μM Calmodulin, 1 mg/mL Casein, 1 mM MgATP, 20 μM DTT, 5 mg/mL glucose, 192 U/mL glucose oxidase, 48 μg/mL catalase. All protein and reagent solutions for each step were prepared in motility buffer (60 mM MOPS, pH 7.0, 25 mM KCl, 1 mM EGTA, 1mM $MgCl_2$). The open ends of the chamber were sealed with vacuum grease and it was placed on an inverted microscope.

Microscopy: Experiments containing GUVs were performed at 22°C on two different inverted TIRF microscopes: (1) a dual-view Leica TIRF microscope with 488 nm Melles Griot 43 series ion laser and 633 nm Optoengine lasers, Photometrics Evolve EMCCD camera, and Metamorph (Molecular Devices) imaging software. We used this setup for all PIP_2-GUV experiments, and acquired images at 1 frame per second for 10 min. (2) Alternatively, a PerkinElmer Nikon Eclipse Ti TIRF with 488 nm, 561 nm, and 640 nm lasers and Volocity image acquisition software was employed. LM-GUV, biotin-PIP_2-GUV, and FCHo PIP_2-GUV movies (and one round of PIP_2-GUV experiments with 80 nM endophilin to control for microscope variability—none found) were acquired with 488 nm

and 640 nm lasers acquiring at 2 frames/minute, and a 561 nm laser acquiring at 2 frames/second.

Experiments containing membrane-coated beads were imaged on a Leica epifluorescence microscope using a 100x oil objective. Movies were recorded under simultaneous epifluorescence and transmission light illumination at RT with an acquisition rate of 2 s/frame, and a movie of 20 min.

QUANTIFICATION AND STATISTICAL ANALYSIS

Image analysis—Events at AF/MT intersections were analyzed for the deformation of the vesicle while at the AF/MT intersection. Deformation was measured by drawing a 1-pixel-wide kymograph along the length of the MT and then measuring the longest and shortest lengths of the GUV over time, along the MT while at the AF intersection. The threshold for "deformed" GUVs was set at 2 standard deviations from the mean of kinesin-1-only longest-divided-by-shortest GUV length changes (designated as β) along the MT while at the AF intersection ($\beta \geq 1.36$). Thus, GUVs with $\beta \geq 1.36$ at an AF/MT intersection were classified as a "deformation" event, unless a membrane extension of diffraction-limited width was pulled along the MT, in which case it was classified as a "tubulation" event. Deformation and tubulation were also assessed for the absolute length of the membrane growth along the MT by subtracting the shortest length from the longest length along the MT while at the AF intersection (as determined by a kymograph drawn along the length of the MT).

Due to the spatial and time resolution of our assay, we are unable to determine whether deformation and tubulation are two parts of the same process, where deformation can lead to tubulation under certain circumstances, or whether they represent two distinct physiological events. In fact, we have very few examples of deformation preceding tubulation, and in the case of Figure 2C (Movie S4), the deformation and tubulation occurred at successive AF/MT intersections. The fact that 60% of GUVs deform in the presence of 0 nM, 8 nM, and 80 nM endophilin while the percentage of tubulation increases from 3% to 34% may indicate that these two processes are not directly linked. Deformation itself has not been characterized in cellular assays, likely due to these same limitations. Note, we did not measure the length/width ratio of the GUV to measure deformation since we were looking at the GUV in TIRF and thus, could not confidently measure the actual GUV length and width. Rather, we quantified deformation by looking at the relative length of the GUV, the bottom ~200 nm of which is illuminated in the TIRF field, with respect to its motile track. Tube elongation velocity was measured for each tubulation event observed, including each tubulation event for every GUV with observed tubulation, whereas the analysis for the longest/shortest or longest-shortest analysis only included the longest tubulation event by a GUV at an individual AF/MT intersection.

Single molecule kinesin-1 (K560) velocities were measured via kymograph under the same experimental conditions as the other reconstitution assays, with no AFs present on patterned stripes. Morphologically dynamic GUVs were not analyzed for their shape change at AF/MT intersections in order to isolate kinesin-1-driven membrane shape changes along the MT. GUVs were also classified as "passing" or "pausing" at AF/MT intersections when already in the process of MT-based transport. A "pause" is classified as a halt in transport

visible by kymograph, thus, a pause ≥2 s in length. Tube elongation persistence time was measured, via a kymograph drawn along the length of the MT, as the length of time between the initiation of tubulation and the first rapid retraction or "snap back" of the tube. Tubulation events that were stabilized by Myo1c at AF intersections, or those where the vesicle body moved toward the tube tip, thereby relieving membrane tension, were not analyzed. Additionally, we adjusted the "dead-time" of the various experiments by limiting the minimum elongation time to 2 s, the minimum detectable by a 1 frame-per-second frame rate. Biotin-PIP_2-GUV pause lengths were limited by the acquisition rate of 1 frame-per-second to a minimum pause of 2 s.

AF-based transport, deformation, and tubulation were quantitated as a fraction of all events in at least 3 fields-of-view across at least 3 different vesicle preps. AF-based deformation and tubulation were quantitated similarly to deformation and tubulation at AF/MT intersections, by drawing a line along the length of the AF and then measuring the length of the vesicle at its longest and shortest length during the course of transport. The thresholds for deformation and tubulation were the same used at AF/MT intersections, where deformation was classified as $\beta \geq 1.36$, and a tubulation event is a membrane extension of a diffraction-limited width. Morphologically dynamic GUVs were designated by observing the GUV shape as it approached the cytoskeleton within the TIRF field. If the GUV showed any hint of having a non-spherical shape (i.e., membrane blebs, extensions, tubes, etc.), then it was classified as "morphologically dynamic," rather than "spherical." Myo1c-driven GUV velocity was quantitated by using a kymograph drawn along the AF-based transport path and measuring the velocity of constant-velocity segments during GUV transport. We normalized the velocity of each segment by the length of time spent at that velocity to obtain the median velocity of 6.0 nm/s (Figure 1E).

Statistical analysis—The software GraphPad Prism was used for all statistical analyses. We used the non-parametric Kolmogorov-Smirnov t test and Kruskal-Wallis ANOVA test with Dunn's multiple comparisons post hoc to compare multiple variables. Boxplots illustrate the 25^{th} and 75^{th} percentiles of the data with a central line at the median, and the whiskers extending to the minimum and maximum points. See figure legends for details about the value and meaning of n for each experiment, as well as the statistical tests used, and the significance as determined by these tests.

Supplementary Material

Refer to Web version on PubMed Central for supplementary material.

Acknowledgments

We thank Tianming Lin, Liqiong Chen, Mariko Tokito, and Dan Safer for excellent technical assistance. Additionally, we thank Erin Masucci for experimental aid, and Michael Woody, Michael Greenberg, Henry Shuman, and other members of the E.M.O., E.L.F.H., and Yale Goldman labs, as well as the Pennsylvania Muscle Institute for helpful suggestions and stimulating conversations. We also appreciate the assistance and expertise of Laurent Blanchoin from Grenoble, France, and Eric Johnston and Brock Peterson from the Singh Center for Nanotechnology at the University of Pennsylvania for help establishing the micropatterned coverslip protocol. Finally, we thank Tobias Baumgart and his laboratory, in particular Zhiming Chen and Jaclyn Robustelli, for expressed and purified endophilin and FCHo-protein and BAR-protein expertise. This work was supported by NIH grants T32 AR053461 (to B.B.M.) and P01 GM087253 (to E.L.F.H. and E.M.O.).

References

1. Huber F, Boire A, López MP, Koenderink GH. Cytoskeletal crosstalk: when three different personalities team up. Curr Opin Cell Biol. 2015; 32:39–47. [PubMed: 25460780]
2. Waterman-Storer CM, Salmon ED. Actomyosin-based retrograde flow of microtubules in the lamella of migrating epithelial cells influences microtubule dynamic instability and turnover and is associated with microtubule breakage and treadmilling. J Cell Biol. 1997; 139:417–434. [PubMed: 9334345]
3. Zajac AL, Goldman YE, Holzbaur ELF, Ostap EM. Local cytoskeletal and organelle interactions impact molecular-motor-driven early endosomal trafficking. Curr Biol. 2013; 23:1173–1180. [PubMed: 23770188]
4. Bartolini F, Gundersen GG. Generation of noncentrosomal microtubule arrays. J Cell Sci. 2006; 119:4155–4163. [PubMed: 17038542]
5. Almeida CG, Yamada A, Tenza D, Louvard D, Raposo G, Coudrier E. Myosin 1b promotes the formation of post-Golgi carriers by regulating actin assembly and membrane remodelling at the *trans*-Golgi network. Nat Cell Biol. 2011; 13:779–789. [PubMed: 21666684]
6. Brandstaetter H, Kendrick-Jones J, Buss F. Myo1c regulates lipid raft recycling to control cell spreading, migration and *Salmonella* invasion. J Cell Sci. 2012; 125:1991–2003. [PubMed: 22328521]
7. Cobbold C, Coventry J, Ponnambalam S, Monaco AP. Actin and microtubule regulation of *trans*-Golgi network architecture, and copper-dependent protein transport to the cell surface. Mol Membr Biol. 2004; 21:59–66. [PubMed: 14668139]
8. Egea G, Serra-Peinado C, Gavilan MP, Rios RM. Cytoskeleton and Golgi-apparatus interactions: a two-way road of function and structure. Cell Health Cytoskelet. 2015; 7:37–54.
9. Gurel PS, Hatch AL, Higgs HN. Connecting the cytoskeleton to the endoplasmic reticulum and Golgi. Curr Biol. 2014; 24:R660–R672. [PubMed: 25050967]
10. Puthenveedu MA, Lauffer B, Temkin P, Vistein R, Carlton P, Thorn K, Taunton J, Weiner OD, Parton RG, von Zastrow M. Sequence-dependent sorting of recycling proteins by actin-stabilized endosomal microdomains. Cell. 2010; 143:761–773. [PubMed: 21111236]
11. Boguslavsky S, Chiu T, Foley KP, Osorio-Fuentealba C, Antonescu CN, Bayer KU, Bilan PJ, Klip A. Myo1c binding to sub-membrane actin mediates insulin-induced tethering of GLUT4 vesicles. Mol Biol Cell. 2012; 23:4065–4078. [PubMed: 22918957]
12. Hunt SD, Townley AK, Danson CM, Cullen PJ, Stephens DJ. Microtubule motors mediate endosomal sorting by maintaining functional domain organization. J Cell Sci. 2013; 126:2493–2501. [PubMed: 23549789]
13. McIntosh BB, Ostap EM. Myosin-I molecular motors at a glance. J Cell Sci. 2016; 129:2689–2695. [PubMed: 27401928]
14. Semiz S, Park JG, Nicoloro SMC, Furcinitti P, Zhang C, Chawla A, Leszyk J, Czech MP. Conventional kinesin KIF5B mediates insulin-stimulated GLUT4 movements on microtubules. EMBO J. 2003; 22:2387–2399. [PubMed: 12743033]
15. Portran D, Gaillard J, Vantard M, Thery M. Quantification of MAP and molecular motor activities on geometrically controlled microtubule networks. Cytoskeleton (Hoboken). 2013; 70:12–23. [PubMed: 23027541]
16. Herold C, Leduc C, Stock R, Diez S, Schwille P. Long-range transport of giant vesicles along microtubule networks. ChemPhysChem. 2012; 13:1001–1006. [PubMed: 22213552]
17. Hokanson DE, Ostap EM. Myo1c binds tightly and specifically to phosphatidylinositol 4,5-bisphosphate and inositol 1,4,5-trisphosphate. Proc Natl Acad Sci USA. 2006; 103:3118–3123. [PubMed: 16492791]
18. Hokanson DE, Laakso JM, Lin T, Sept D, Ostap EM. Myo1c binds phosphoinositides through a putative pleckstrin homology domain. Mol Biol Cell. 2006; 17:4856–4865. [PubMed: 16971510]
19. Hendricks AG, Perlson E, Ross JL, Schroeder HW III, Tokito M, Holzbaur ELF. Motor coordination via a tug-of-war mechanism drives bidirectional vesicle transport. Curr Biol. 2010; 20:697–702. [PubMed: 20399099]

20. McIntosh BB, Holzbaur ELF, Ostap EM. Control of the initiation and termination of kinesin-1-driven transport by myosin-Ic and nonmuscle tropomyosin. Curr Biol. 2015; 25:523–529. [PubMed: 25660542]
21. Bai J, Hu Z, Dittman JS, Pym ECG, Kaplan JM. Endophilin functions as a membrane-bending molecule and is delivered to endocytic zones by exocytosis. Cell. 2010; 143:430–441. [PubMed: 21029864]
22. Farsad K, Ringstad N, Takei K, Floyd SR, Rose K, De Camilli P. Generation of high curvature membranes mediated by direct endophilin bilayer interactions. J Cell Biol. 2001; 155:193–200. [PubMed: 11604418]
23. Gallop JL, Jao CC, Kent HM, Butler PJG, Evans PR, Langen R, McMahon HT. Mechanism of endophilin N-BAR domain-mediated membrane curvature. EMBO J. 2006; 25:2898–2910. [PubMed: 16763559]
24. Zhu C, Das SL, Baumgart T. Nonlinear sorting, curvature generation, and crowding of endophilin N-BAR on tubular membranes. Biophys J. 2012; 102:1837–1845. [PubMed: 22768939]
25. Chen Z, Zhu C, Kuo CJ, Robustelli J, Baumgart T. The N-terminal amphipathic helix of endophilin does not contribute to its molecular curvature generation capacity. J Am Chem Soc. 2016; 138:14616–14622. [PubMed: 27755867]
26. Vinatier J, Herzog E, Plamont MA, Wojcik SM, Schmidt A, Brose N, Daviet L, El Mestikawy S, Giros B. Interaction between the vesicular glutamate transporter type 1 and endophilin A1, a protein essential for endocytosis. J Neurochem. 2006; 97:1111–1125. [PubMed: 16606361]
27. Weston MC, Nehring RB, Wojcik SM, Rosenmund C. Interplay between VGLUT isoforms and endophilin A1 regulates neurotransmitter release and short-term plasticity. Neuron. 2011; 69:1147–1159. [PubMed: 21435559]
28. Suetsugu S, Kurisu S, Takenawa T. Dynamic shaping of cellular membranes by phospholipids and membrane-deforming proteins. Physiol Rev. 2014; 94:1219–1248. [PubMed: 25287863]
29. Angers A, Ramjaun AR, McPherson PS. The HECT domain ligase itch ubiquitinates endophilin and localizes to the *trans*-Golgi network and endosomal system. J Biol Chem. 2004; 279:11471–11479. [PubMed: 14684745]
30. Neumann S, Schmid SL. Dual role of BAR domain-containing proteins in regulating vesicle release catalyzed by the GTPase, dynamin-2. J Biol Chem. 2013; 288:25119–25128. [PubMed: 23861397]
31. Roux A, Uyhazi K, Frost A, De Camilli P. GTP-dependent twisting of dynamin implicates constriction and tension in membrane fission. Nature. 2006; 441:528–531. [PubMed: 16648839]
32. Simunovic M, Manneville JB, Renard HF, Evergren E, Raghunathan K, Bhatia D, Kenworthy AK, Voth GA, Prost J, McMahon HT, et al. Friction mediates scission of tubular membranes scaffolded by BAR proteins. Cell. 2017; 170:172–184. e11. [PubMed: 28648660]
33. Kjaerulff O, Brodin L, Jung A. The structure and function of endophilin proteins. Cell Biochem Biophys. 2011; 60:137–154. [PubMed: 21184288]
34. Frost A, Perera R, Roux A, Spasov K, Destaing O, Egelman EH, De Camilli P, Unger VM. Structural basis of membrane invagination by F-BAR domains. Cell. 2008; 132:807–817. [PubMed: 18329367]
35. Henne WM, Kent HM, Ford MGJ, Hegde BG, Daumke O, Butler PJG, Mittal R, Langen R, Evans PR, McMahon HT. Structure and analysis of FCHo2 F-BAR domain: a dimerizing and membrane recruitment module that effects membrane curvature. Structure. 2007; 15:839–852. [PubMed: 17540576]
36. Henne WM, Boucrot E, Meinecke M, Evergren E, Vallis Y, Mittal R, McMahon HT. FCHo proteins are nucleators of clathrin-mediated endocytosis. Science. 2010; 328:1281–1284. [PubMed: 20448150]
37. Uezu A, Umeda K, Tsujita K, Suetsugu S, Takenawa T, Nakanishi H. Characterization of the EFC/F-BAR domain protein, FCHO2. Genes Cells. 2011; 16:868–878. [PubMed: 21762413]
38. Nelson SR, Trybus KM, Warshaw DM. Motor coupling through lipid membranes enhances transport velocities for ensembles of myosin Va. Proc Natl Acad Sci USA. 2014; 111:E3986–E3995. [PubMed: 25201964]

39. Rai A, Pathak D, Thakur S, Singh S, Dubey AK, Mallik R. Dynein clusters into lipid microdomains on phagosomes to drive rapid transport toward lysosomes. Cell. 2016; 164:722–734. [PubMed: 26853472]
40. Levental I, Veatch S. The continuing mystery of lipid rafts. J Mol Biol. 2016; 428:4749–4764. [PubMed: 27575334]
41. Yin HL, Janmey PA. Phosphoinositide regulation of the actin cytoskeleton. Annu Rev Physiol. 2003; 65:761–789. [PubMed: 12471164]
42. Yamada A, Mamane A, Lee-Tin-Wah J, Di Cicco A, Prévost C, Lévy D, Joanny JF, Coudrier E, Bassereau P. Catch-bond behaviour facilitates membrane tubulation by non-processive myosin 1b. Nat Commun. 2014; 5:3624. [PubMed: 24709651]
43. Corbin JA, Evans JH, Landgraf KE, Falke JJ. Mechanism of specific membrane targeting by C2 domains: localized pools of target lipids enhance Ca^{2+} affinity. Biochemistry. 2007; 46:4322–4336. [PubMed: 17367165]
44. Gagescu R, Demaurex N, Parton RG, Hunziker W, Huber LA, Gruenberg J. The recycling endosome of Madin-Darby canine kidney cells is a mildly acidic compartment rich in raft components. Mol Biol Cell. 2000; 11:2775–2791. [PubMed: 10930469]
45. McMurray, WC. Phospholipids in subcellular organelles and membranes. In: Ansell, GB.Hawthorne, JN., Dawson, RMC., editors. Form and Function of Phospholipids. Elsevier; 1973. p. 205-251.
46. Mondal M, Mesmin B, Mukherjee S, Maxfield FR. Sterols are mainly in the cytoplasmic leaflet of the plasma membrane and the endocytic recycling compartment in CHO cells. Mol Biol Cell. 2009; 20:581–588. [PubMed: 19019985]
47. Stahelin RV, Rafter JD, Das S, Cho W. The molecular basis of differential subcellular localization of C2 domains of protein kinase C-α and group IVa cytosolic phospholipase A2. J Biol Chem. 2003; 278:12452–12460. [PubMed: 12531893]
48. Sampaio JL, Gerl MJ, Klose C, Ejsing CS, Beug H, Simons K, Shevchenko A. Membrane lipidome of an epithelial cell line. Proc Natl Acad Sci USA. 2011; 108:1903–1907. [PubMed: 21245337]
49. McKenna JMD, Ostap EM. Kinetics of the interaction of myo1c with phosphoinositides. J Biol Chem. 2009; 284:28650–28659. [PubMed: 19706607]
50. Du W, Su QP, Chen Y, Zhu Y, Jiang D, Rong Y, Zhang S, Zhang Y, Ren H, Zhang C, et al. Kinesin 1 drives autolysosome tubulation. Dev Cell. 2016; 37:326–336. [PubMed: 27219061]
51. Koster G, VanDuijn M, Hofs B, Dogterom M. Membrane tube formation from giant vesicles by dynamic association of motor proteins. Proc Natl Acad Sci USA. 2003; 100:15583–15588. [PubMed: 14663143]
52. Roux A, Cappello G, Cartaud J, Prost J, Goud B, Bassereau P. A minimal system allowing tubulation with molecular motors pulling on giant liposomes. Proc Natl Acad Sci USA. 2002; 99:5394–5399. [PubMed: 11959994]
53. Schroeder HW III, Hendricks AG, Ikeda K, Shuman H, Rodionov V, Ikebe M, Goldman YE, Holzbaur ELF. Force-dependent detachment of kinesin-2 biases track switching at cytoskeletal filament intersections. Biophys J. 2012; 103:48–58. [PubMed: 22828331]
54. Shaklee PM, Idema T, Bourel-Bonnet L, Dogterom M, Schmidt T. Kinesin recycling in stationary membrane tubes. Biophys J. 2010; 99:1835–1841. [PubMed: 20858428]
55. Svoboda K, Block SM. Force and velocity measured for single kinesin molecules. Cell. 1994; 77:773–784. [PubMed: 8205624]
56. Koster G, Cacciuto A, Derényi I, Frenkel D, Dogterom M. Force barriers for membrane tube formation. Phys Rev Lett. 2005; 94:068101. [PubMed: 15783778]
57. Leduc C, Campàs O, Zeldovich KB, Roux A, Jolimaitre P, Bourel-Bonnet L, Goud B, Joanny JF, Bassereau P, Prost J. Cooperative extraction of membrane nanotubes by molecular motors. Proc Natl Acad Sci USA. 2004; 101:17096–17101. [PubMed: 15569933]
58. Greenberg MJ, Lin T, Goldman YE, Shuman H, Ostap EM. Myosin IC generates power over a range of loads via a new tension-sensing mechanism. Proc Natl Acad Sci USA. 2012; 109:E2433–E2440. [PubMed: 22908250]

59. Laakso JM, Lewis JH, Shuman H, Ostap EM. Myosin I can act as a molecular force sensor. Science. 2008; 321:133–136. [PubMed: 18599791]
60. Kee AJ, Yang L, Lucas CA, Greenberg MJ, Martel N, Leong GM, Hughes WE, Cooney GJ, James DE, Ostap EM, et al. An actin filament population defined by the tropomyosin Tpm3.1 regulates glucose uptake. Traffic. 2015; 16:691–711. [PubMed: 25783006]
61. Pathak D, Mallik R. Lipid - motor interactions: soap opera or symphony? Curr Opin Cell Biol. 2017; 44:79–85. [PubMed: 27697416]
62. Castoldi M, Popov AV. Purification of brain tubulin through two cycles of polymerization-depolymerization in a high-molarity buffer. Protein Expr Purif. 2003; 32:83–88. [PubMed: 14680943]
63. Pierce, DW., Vale, RD. Assaying processive movement of kinesin by fluorescence microscopy. In: Valee, RB., editor. Methods in Enzymology: Molecular Motors and the Cytoskeleton, Part B. Academic Press; 1998. p. 154-171.
64. Pyrpassopoulos S, Feeser EA, Mazerik JN, Tyska MJ, Ostap EM. Membrane-bound myo1c powers asymmetric motility of actin filaments. Curr Biol. 2012; 22:1688–1692. [PubMed: 22863317]
65. Capraro BR, Shi Z, Wu T, Chen Z, Dunn JM, Rhoades E, Baumgart T. Kinetics of endophilin N-BAR domain dimerization and membrane interactions. J Biol Chem. 2013; 288:12533–12543. [PubMed: 23482561]
66. Chen Z, Chang K, Capraro BR, Zhu C, Hsu CJ, Baumgart T. Intradimer/intermolecular interactions suggest autoinhibition mechanism in endophilin A1. J Am Chem Soc. 2014; 136:4557–4564. [PubMed: 24568626]
67. Putkey JA, Slaughter GR, Means AR. Bacterial expression and characterization of proteins derived from the chicken calmodulin cDNA and a calmodulin processed gene. J Biol Chem. 1985; 260:4704–4712. [PubMed: 2985564]
68. Chen Z, Shi Z, Baumgart T. Regulation of membrane-shape transitions induced by I-BAR domains. Biophys J. 2015; 109:298–307. [PubMed: 26200865]
69. Azioune A, Carpi N, Tseng Q, Théry M, Piel M. Protein micropatterns: a direct printing protocol using deep UVs. Methods Cell Biol. 2010; 97:133–146. [PubMed: 20719269]
70. Boujemaa-Paterski R, Galland R, Suarez C, Guérin C, Théry M, Blanchoin L. Directed actin assembly and motility. Methods Enzymol. 2014; 540:283–300. [PubMed: 24630113]
71. Reymann AC, Guérin C, Théry M, Blanchoin L, Boujemaa-Paterski R. Geometrical control of actin assembly and contractility. Methods Cell Biol. 2014; 120:19–38. [PubMed: 24484655]
72. Kron SJ, Spudich JA. Fluorescent actin filaments move on myosin fixed to a glass surface. Proc Natl Acad Sci USA. 1986; 83:6272–6276. [PubMed: 3462694]

Highlights

- In vitro cytoskeletal arrays can be engineered to investigate membrane tubulation
- Kinesin-1 and Myo1c coordinate to deform vesicles along cytoskeletal arrays
- BAR-domain proteins enhance kinesin- and myosin-driven membrane tubulation
- Lipid composition modulates membrane remodeling by BAR-domain proteins and motors

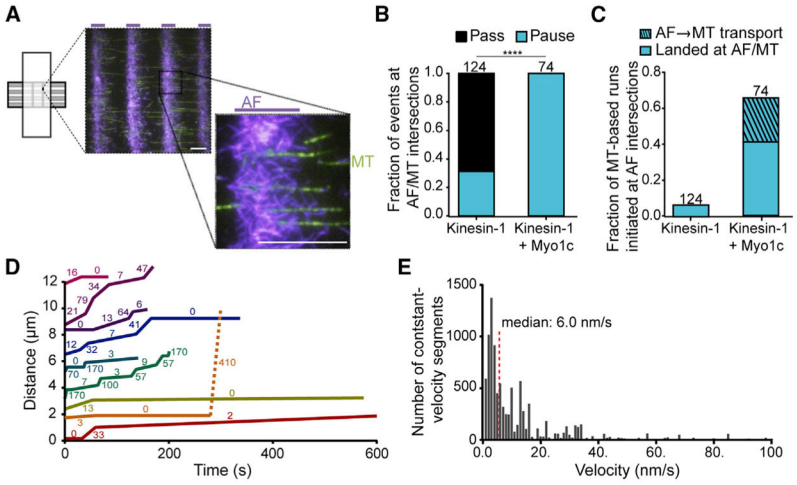

Figure 1. Kinesin-1 and Myo1c Transport PIP_2-GUVs along Microtubule (MT) and Actin Filament (AF) Tracks

(A) We engineered patterned cytoskeletal arrays composed of sparse MTs (green) crossing beneath dense AF (purple) regions to mimic complex physiological cytoskeletal networks. The inset shows intersections at higher magnification. The purple lines above images indicate micropatterned regions of AF binding. Scale bars, 10 μm.

(B) Graph of the fraction of PIP_2-GUVs motile along MTs containing kinesin-1 only or kinesin-1+Myo1c that pass or pause at AF intersections. The total number of events observed at AF/MT intersections from 17 (kinesin-1-only) and 16 (kinesin-1+Myo1c) different PIP_2-GUV preparations is written above each bar. Kolmogorov-Smirnov test, ****$p \leq 0.0001$.

(C) Graph of the fraction of PIP_2-GUVs motile along MTs that initiate their MT-based motility either at AF intersections (solid bars) or by switching from AF-based to MT-based transport (striped bar). See also Figure S1 and Movie S1.

(D) PIP_2-bound Myo1c transports GUVs along AF tracks. Distance versus time graph showing example trajectories of Myo1c-driven PIP_2-GUV motility along AFs during 600-s acquisitions acquired at 1 frame/s. The velocity (nm/s) of each constant-velocity segment appears next to each track. The orange line depicts a transition from AF-based (solid line) to MT-based (dashed line) motility. See also Movie S2.

(E) Graph of the time-weighted, constant-velocity segments of Myo1c-driven PIP_2-GUV motility. The median velocity is 6.0 nm/s and indicated by the red dashed line; n = 109 vesicles from 17 (kinesin-1-only) and 16 (kinesin-1+Myo1c) different GUV preparations.

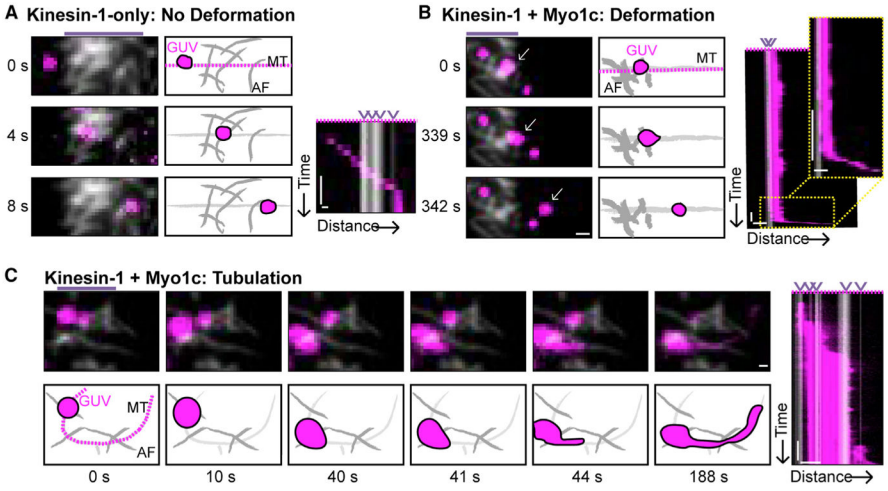

D

Vesicle Example	GUV length along MT: Shortest (μm)	Longest (μm)	β = longest / shortest	Tube elongation?	GUV morphology (before / after)
2A	0.56	0.66	1.17	No	Spherical / Non-deformed
2B	0.61	1.15	1.86	No	Spherical / Deformed
2C	0.98	4.78	4.89	Yes	Spherical / Tubulated

Figure 2. Kinesin-1 and Myo1c Together Deform PIP_2-GUVs at AF/MT Intersections along MTs

(A) PIP_2-GUVs with only kinesin-1 bound are largely non-deformed as they encounter AF intersections. Time series, illustration, and kymograph showing a kinesin-1-transported GUV with unchanging shape in relation to the MT as it encountered four AF/MT intersections. See (D) for more detailed deformation analysis of GUVs shown in (A)–(C). AF intersections are indicated by purple arrowheads above the kymograph, and micropatterned regions of AF binding are indicated by purple lines above the time-series images. The magenta dotted line in the illustration indicates the line the kymograph was drawn along. Scale bars, 1 μm, 5 s. See also Movie S3.

(B) PIP_2-GUVs with kinesin-1+Myo1c typically deform at AF/MT intersections. Time series, illustration, and kymograph showing an example deformation event. The inset to the kymograph magnifies the kymograph highlighting the transition to MT-based transport. AF intersections are indicated by purple arrowheads above the kymograph, and micropatterned regions of AF binding are indicated by purple lines above the time-series images. The magenta dotted line in the illustration indicates the line the kymograph was drawn along. White arrows indicate GUV of interest. Scale bars, 5 μm, 25 s (note scale differences between figures). See also Movie S3.

(C) PIP_2-GUVs with kinesin-1+Myo1c rarely tubulate at AF/MT intersections. A GUV deforms and tubulates at successive AF/MT intersections. Time series, illustration, and kymograph showing an example tubulation event where $\beta \geq 1.36$ and a tube of diffraction-limited width is pulled along the MT. AF intersections are indicated by purple arrowheads above the kymograph, and micropatterned regions of AF binding are indicated by purple lines above the time-series images. The magenta dotted line in the illustration indicates the line the kymograph was drawn along. Scale bars, 5 μm, 25 s. See also Movie S4.

(D) Parameters used to evaluate GUV shape change. The length of the GUV (μm) along the MT at AF intersections was determined from a kymograph drawn along the MT and used to find β (longest/shortest). Deformed GUVs are defined as β ≥1.36 in the absence of a diffraction-limited tube, as determined by a kymograph drawn perpendicular to the MT, as seen in (B). Tubulated GUVs are defined as β ≥1.36 with a membrane extension of diffraction-limited width pulled along the MT, as seen in (C). GUV morphology before landing in the cytoskeleton and after navigation of the AF intersection is also listed.

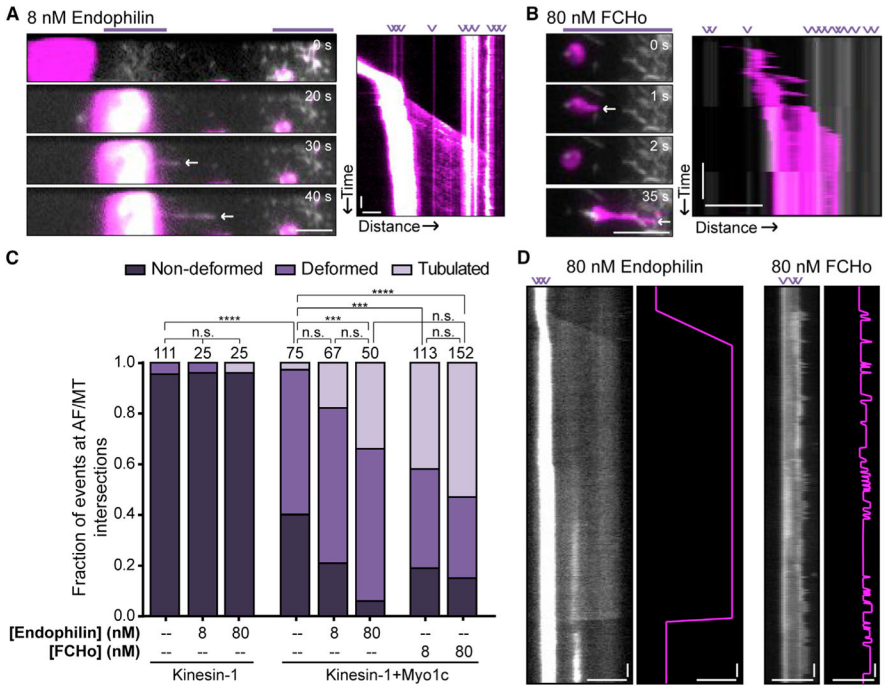

Figure 3. BAR Proteins Endophilin and FCHo Facilitate Tubulation of Kinesin-1+Myo1c GUVs along MT Tracks at AF Intersections

(A) PIP_2-GUVs show enhanced frequency of tubulation along MTs, at AF intersections, and in the presence of Myo1c and the BAR proteins endophilin or FCHo. Example time series and kymograph of a PIP_2-GUV that is motile along the MT until it halts in the micropatterned regions of AF binding (purple lines above the time series). Kinesin-1 pulls a membrane tube along the MT, facilitated by the presence of 8 nM endophilin. The time series is cropped to illustrate the initiation of tubulation. See Movie S5 to observe the entire tubulation event. AF intersections are indicated by purple arrowheads above the kymograph. White arrows in the time series indicate the tip of the elongating tube. Scale bars, 5 μm, 10 s. See also Movie S5 and Figure S2.

(B) Example time series and kymograph of a PIP_2-GUV tubulation facilitated by the presence of 80 nM FCHo. AF intersections are indicated by purple arrowheads above the kymograph, and the micropatterned regions of AF binding are represented by the purple line above the time series. Note that the elongating tubes are stabilized by interaction with AF intersections. White arrows in the time series indicate the tip of the rapidly elongating and rapidly retracting tube. Scale bars, 5 μm, 10 s. See also Movie S6.

(C) Graph showing the percentage of events at AF/MT intersections that are non-deformed (dark purple), deformed (medium purple), or tubulated (light purple). Kinesin-1-only PIP_2-GUVs remain non-deformed in the presence of endophilin. PIP_2-GUVs containing both kinesin-1 and Myo1c show a concentration-dependent increase in the fraction of tubulation events upon addition of endophilin or FCHo. Endophilin (80 nM) significantly increased the frequency of tubulation in the presence of both kinesin-1 and Myo1c, and FCHo (80 nM) appeared to further increase this frequency of tubulation. The number of observed events at AF/MT intersections is written above each bar from ≥6 different GUV preparations and ≥6

experimental chambers. ***$p \leq 0.001$, ****$p \leq 0.0001$ via Kruskal-Wallis with Dunn's multiple comparisons. n.s., not significant.

(D) Endophilin- and FCHo-facilitated tubulation along MTs when tethered at AF intersections. Endophilin-facilitated kinesin-1-driven tubulation elongates at a slower velocity but results in longer tube lengths with increased persistence times. Alternatively, FCHo-facilitated kinesin-1-driven tubulation events have higher elongation velocities and shorter persistence times, resulting in shorter tubes along MTs. Each kymograph is skeletonized in pink to clearly show tubulation and tube-catastrophe events. AF intersections are indicated by purple arrowheads above the kymograph. These kymographs are scaled the same in distance and time for easy comparison. Scale bars, 5 μm, 10 s.

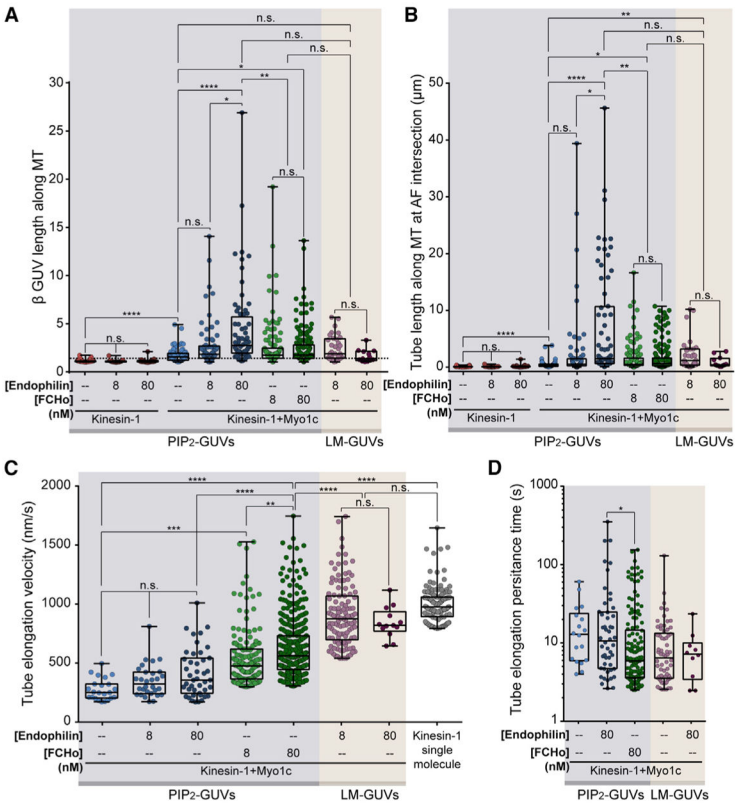

Figure 4. BAR Proteins and Lipid Composition Modulate Kinesin-1-Driven Tubulation along MTs at AF Intersections

(A) Graph comparing the kinesin-1-driven deformation (β) of PIP_2-GUVs (light blue background) and LM-GUVs (light tan background) ± Myo1c, endophilin, and/or FCHo. Addition of Myo1c increases deformation over kinesin-1-only experiments. Endophilin and FCHo further increase kinesin-1+Myo1c PIP_2-GUV deformation. LM-GUVs with kinesin-1+Myo1c do not increase the deformation over that of PIP_2-GUVs, even when endophilin is added. *p ≤ 0.05, **p ≤ 0.01, ****p ≤ 0.0001 via Kruskal-Wallis with Dunn's multiple comparisons; where the significance bar goes between two linked datasets, the datasets were tested individually but shown linked for simplicity.

(B) Graph of GUV tube length (longest minus shortest) as the Myo1c-tethered GUV is elongated along the MT by kinesin-1. There are significantly longer kinesin-1-driven PIP_2-GUV tubulation events in the presence of endophilin and Myo1c compared to kinesin-1 only ± endophilin. Although FCHo increases the length of tubes elongated by kinesin-1 in the presence of Myo1c, these tubes are significantly shorter than endophilin-facilitated tubes. Kinesin-1+Myo1c LM-GUVs ± endophilin are significantly longer than PIP_2-GUVs containing kinesin-1+Myo1c. *p ≤ 0.05, **p ≤ 0.01, ****p ≤ 0.0001 via Kruskal-Wallis with Dunn's multiple comparisons.

(C) Graph of velocities (nm/s) of kinesin-1-driven tube elongation compared to kinesin-1 single-molecule velocities (gray dots to the far right) under the same experimental conditions. Endophilin and FCHo increase PIP_2-GUV tube-elongation velocities. FCHo-stimulated PIP_2-GUV tube-elongation velocities are significantly slower than single-molecule kinesin-1 velocities, whereas LM-GUVs ± endophilin elongate at velocities not

significantly different from kinesin-1 single molecules. **p ≤ 0.01, ***p ≤ 0.001, ****p ≤ 0.0001 via Kruskal-Wallis with Dunn's multiple comparisons.

(D) The persistence of elongating tubes was plotted as the log of the time between initiation of tubulation along the MT and the time when the growing tube rapidly shortens. On PIP_2-GUVs, endophilin stabilizes growing tubes significantly longer than FCHo and experiments with no BAR proteins present. Tubes stabilized at the tip by Myo1c attachment to an AF intersection or when the GUV body moved toward the tip to relieve tension were not included in these analyses. *p ≤0.05, Kruskal-Wallis.

Data are plotted as a box plot where error bars show the range in values (smallest to largest) and the box indicates the interquartile range (middle 50% of data), with the median indicated by the central line.

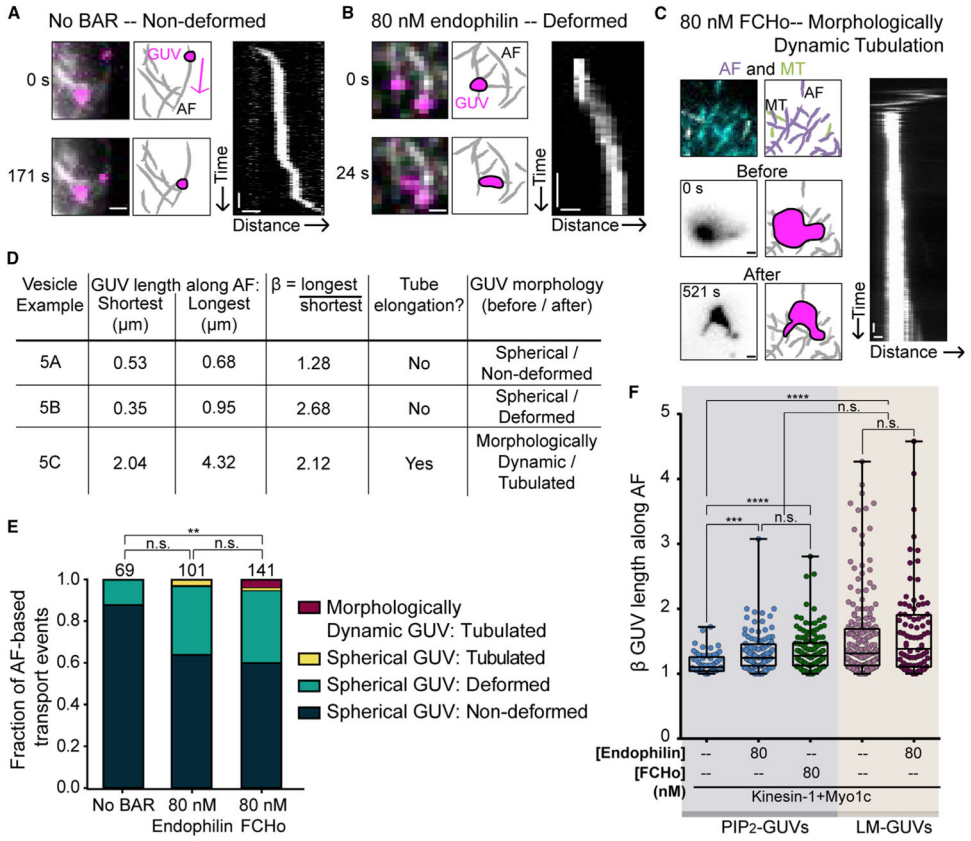

Vesicle Example	GUV length along AF: Shortest (μm)	Longest (μm)	β = longest / shortest	Tube elongation?	GUV morphology (before / after)
5A	0.53	0.68	1.28	No	Spherical / Non-deformed
5B	0.35	0.95	2.68	No	Spherical / Deformed
5C	2.04	4.32	2.12	Yes	Morphologically Dynamic / Tubulated

Figure 5. Myo1c-Driven GUV Deformation and Tubulation along AFs Are Modulated by BAR Proteins

(A) In the absence of BAR proteins, 88% of Myo1c-driven PIP_2-GUVs transported along AFs are non-deformed. The Myo1c-driven transport event in which the first and last frames of motility are shown with the corresponding illustration and kymograph. The magenta arrow indicates the direction of AF-based motility. See (D) for parameters of vesicle shape change with respect to the AF track. Scale bars, 1 μm, 20 s.

(B) PIP_2-GUVs with kinesin-1+Myo1c and 80 nM endophilin show increased deformation and tubulation as they are transported along AFs by Myo1c. Deformation event with corresponding illustrations and kymograph in which $\beta \geq 1.36$ but the membrane is not tubulated. See (D) for GUV shape parameters. Scale bars, 1 μm, 20 s.

(C) 3% of all FCHo-bound PIP_2-GUVs that interacted with AFs showed a morphologically dynamic shape before engaging with, and tubulating along, AFs by Myo1c. A morphologically dynamic GUV tubulation event showing the non-spherical GUV morphology “before” landing on the AF cytoskeleton and “after” tubulation occurred, both in inverted contrast. The cytoskeleton is shown separately from the GUV, and illustrations and kymograph are also included. See (D) for GUV shape parameters. Scale bars, 1 μm, 20 s.

(D) Parameters used to evaluate GUV shape change. Comparable to MT-based deformation analysis, the dimensions of the GUV along the AF during motility were determined from a kymograph drawn along the AF-based motility path, and used to find β. Deformed GUVs are defined as $\beta \geq 1.36$ in the absence of tubulation, as determined by a kymograph drawn

perpendicular to the AFs, as seen in (B). Tubulated GUVs have $\beta \geq 1.36$ with a membrane extension of diffraction-limited width pulled along the AF, as seen in (C).

(E) AF-based transported GUV shape before interacting with the cytoskeleton (spherical or morphologically dynamic) and morphology after Myo1c-driven transport along AFs (non-deformed, deformed, or tubulated). FCHo (80 nM) significantly increased the frequency of deformation and tubulation along AFs. Endophilin (80 nM) resulted in a similar distribution of AF-based membrane remodeling morphologies, but this condition is not significantly different from either the no-BAR-protein or 80 nM FCHo conditions (Kruskal-Wallis with Dunn's multiple comparisons, $^{**}p \leq 0.01$). Total numbers of motile GUVs analyzed for their motility along AFs are listed above each column.

(F) Spherical Myo1c-transported PIP_2-GUVs (light blue background) are significantly more deformed (β) along AFs in the presence of either 80 nM endophilin or 80 nM FCHo (morphologically dynamic GUVs were excluded). All vesicles are in the presence of both kinesin-1 and Myo1c. LM-GUVs ± endophilin (light tan background) deform along AFs significantly more than PIP_2-GUVs. Statistical testing by Kruskal-Wallis with Dunn's multiple comparisons, $^{***}p \leq 0.001$, $^{****}p \leq 0.0001$. Data are plotted as a box plot where error bars show the range in values (smallest to largest) and the box indicates the interquartile range (middle 50% of data), with the median indicated by the central line.

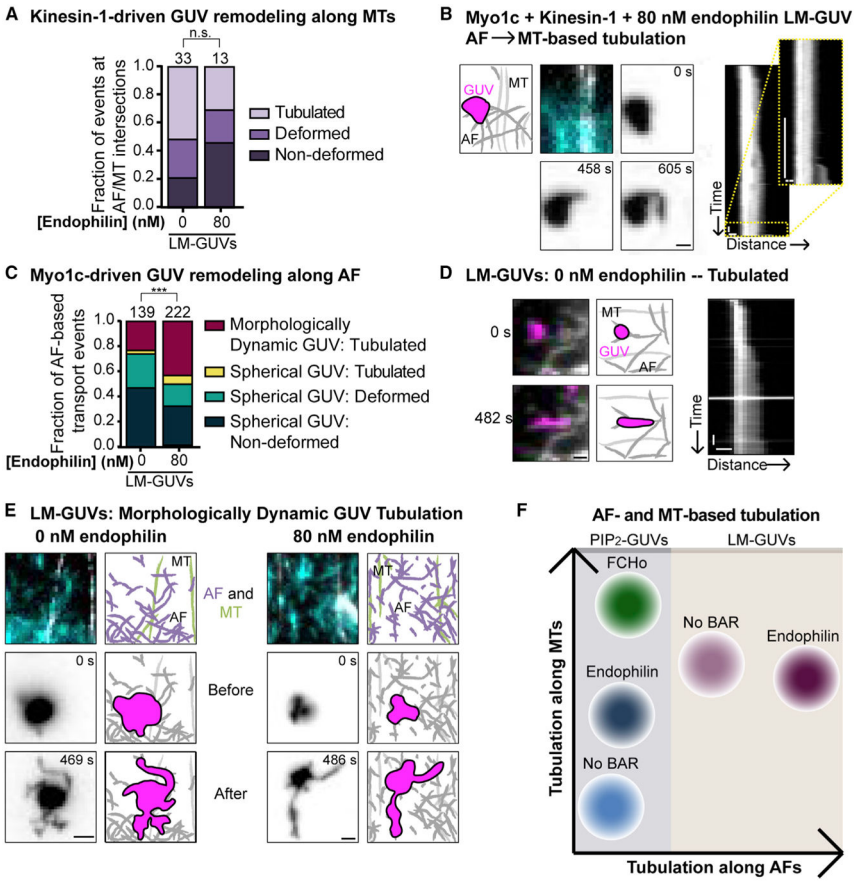

Figure 6. A Physiological Lipid Mixture (LM-GUVs) Promotes Tubulation along Both MTs and AFs

(A) Graph showing the percentage of events at AF/MT intersections that are non-deformed (dark purple), deformed (medium purple), or tubulated (light purple). There is significantly more tubulation by kinesin-1+Myo1c LM-GUVs than PIP_2-GUVs along MTs (compare to Figure 3C). There is no significant difference in the amount of LM-GUV tubulation along MTs ± endophilin. The total number of vesicle events at AF/MT intersections is listed above each column.

(B) LM-GUV tubulation along AFs and MTs in the presence of kinesin-1+Myo1c and 80 nM endophilin. A GUV landed on AFs and was tubulated by Myo1c but then switched to kinesin-1-driven MT-based tubulation. Time series with the AF and MT cytoskeleton, and the LM-GUV morphology before tubulation (0 s), during AF-based tubulation (458 s), and after MT-based tubulation (605 s), in inverted contrast. The corresponding kymographs show AF-based tubulation (left) and MT-based tubulation (right). Scale bars, 1 μm, 20 s. See also Movie S7.

(C) Graph showing the percentage of AF-based transported GUVs that are non-deformed (dark blue), deformed (turquoise), or tubulated along AFs (yellow or burgundy). GUV shape before tubulating along AF was classified as spherical (yellow) or morphologically dynamic (burgundy). Spherical and morphologically dynamic LM-GUVs tubulate more frequently than PIP_2-GUVs (compare to Figure 5E). Endophilin increases LM-GUV tubulation along

AFs. The total number of AF-based motile GUVs analyzed is listed above each column. Kruskal-Wallis with Dunn's multiple comparisons, ***$p \leq 0.001$.

(D) LM-GUVs in the absence of 80 nM endophilin were more deformed and tubulated than PIP_2-GUVs, and showed an increased dynamic morphology. Example tubulation event of an LM-GUV, in the absence of endophilin, shown before (0 s) and after (482 s) tubulation, with the corresponding kymograph. Scale bars, 1 μm, 20 s. See also Movie S8.

(E) A large percentage of LM-GUVs ± 80 nM endophilin were morphologically dynamic in shape and tubulated along AFs. These examples show the cytoskeleton, GUV shape immediately before landing on AFs, and GUV morphology after tubulation in the absence and presence of 80 nM endophilin, with LM-GUVs shown in inverted contrast. Scale bars, 2 μm. See also Movie S9.

(F) Summary of AF-based and MT-based tubulation. Increased tubulation along MTs by kinesin-1 can be stimulated by addition of the BAR proteins endophilin or FCHo to PIP_2-rich GUVs, or by increasing the physiological complexity of lipid head groups within the membrane (LM-GUVs). Myo1c-driven tubulation along AFs is preferentially stimulated by changing the lipid composition, rather than by the presence of BAR proteins alone.

Table 1

GUV Lipid Compositions

Type of Lipid	PIP_2-GUVs (%)	Biotin-PIP_2-GUVs (%)	LM-GUVs (%)	CH-LM-GUVs (%)
Rho-PE	0.5	0.5	0.5	0.5
DGS-NTA(Ni)	2.5	2.5	2.5	2.5
$PI(4,5)P_2$	20.5	20.5	3.0	2.0
PC	76.5	66.5	18.4	10.5
PE	–	–	43.3	29.5
PS	–	–	18.4	21.0
PI	–	–	9.2	4.5
Sphingomyelin	–	–	4	4.5
Cholesterol	–	–	–	25.0
Biotin-PE	–	10	–	–

Mol% of each lipid included in the three different lipid mixtures. Rho-PE: 18:1 1,2-dioleoyl-*sn*-glycero-3-phosphoethanolamine-*N*-(lissamine rhodamine B sulfonyl) (ammonium salt); DGS-NTA(Ni): 18:1 1,2-dioleoyl-*sn*-glyc-ero-3-[(*N*-(5-amino-1-carboxypentyl)iminodiacetic acid)succinyl] (nickel salt); $PI(4,5)P_2$: porcine brain L-α-phosphatidylinositol-4,5-bisphosphate; PC: 18:1 (Δ9-Cis) 1,2-dioleoyl-*sn*-glycero-3-phosphocholine; PE: 18:1 (Δ9-Cis) 1,2-dioleoyl-*sn*-glycero-3-phosphoethanolamine; PS: 18:1 1,2-dioleoyl-*sn*-glycero-3-phospho-L-serine; PI: 18:1 1,2-dioleoyl-*sn*-glycero-3-phospho-(1′-myo-inositol) (ammonium salt); sphingomyelin: porcine brain derived; cholesterol: ovine wool derived; biotin-PE: 1,2-dioleoyl-*sn*-glycero-3-phosphoethanolamine-*N*-(cap biotinyl) (sodium salt).